Novel hybrid thermochemical cycles for low-grade heat storage and autothermal power generation: a thermodynamic study

Alexis Godefroy, Maxime Perier-Muzet, Nathalie Mazet

Novel hybrid thermochemical cycles for low-grade heat storage and autothermal power generation: a thermodynamic study

Alexis Godefroy[1,2], Maxime Perier-Muzet[1,2], Nathalie Mazet[1*]

[1]CNRS-PROMES Laboratoire PROcédés, Matériaux et Energie Solaire, Tecnosud, Rambla de la Thermodynamique, 66100 Perpignan, France

[2]UPVD Université de Perpignan Via Domitia, 52 Avenue Paul Alduy, 66100 Perpignan, France

[*] Corresponding author

E-mail addresses: alexis.godefroy@univ-perp.fr (A. Godefroy), maxime.perier-muzet@univ-perp.fr (M. Perier-Muzet), mazet@univ-perp.fr (N. Mazet).

Abstract

The principle of hybridizing a solid/gas thermochemical refrigeration cycle with a power cycle is extended to two novel hybrid cycles (called operating modes). They can be driven by low-grade heat, and they allow storing this energy and converting it predominantly into mechanical power. For this purpose, they integrate an original autothermal power production during their discharging step, which is deeply analyzed. In addition, depending on the operating mode, power can be produced in both charging and discharging steps and an additional cold production can be provided. A deep thermodynamic study was carried out to assess the performance of these cycles, for 103 solid/gas pairs. These cycles allow converting low-grade heat sources from 87 °C to 250 °C. The maximal energy and exergy efficiencies for power and cold cogeneration are 0.24 and 0.40, respectively, and the maximal exergy density is 722 kJ/kg_{NH3}. The part of power production reaches 62% (when it occurs only in discharging step) to 78% (when it occurs in both steps).

Keywords: thermochemical cycles, sorption, hybrid cycles, power and refrigeration cogeneration, thermal storage, thermodynamic analysis

Nomenclature

Symbols

c	Mass heat capacity at constant pressure ($J.kg^{-1}.K^{-1}$)
$C, \bar{C}$	Molar heat capacity at constant pressure ($J.mol^{-1}.K^{-1}$)
COP	Coefficient Of Performance ($-$)
$\Delta_r H$	Reaction enthalpy ($J.mol^{-1}$)
$\Delta_r S$	Reaction entropy ($J.mol^{-1}.K^{-1}$)
ΔS_{vap}	Vaporization entropy ($J.mol^{-1}.K^{-1}$)
ΔT	Temperature pinch (K)
ΔX	Variation range of reaction advancement ($-$)
ex	Specific exergy quantity ($J.kg^{-1}$)
Ex	Exergy quantity (J)
h	Specific enthalpy ($J.kg^{-1}$)
L_{vap}	Vaporization enthalpy ($J.mol^{-1}$)
m	Mass (kg)
M	Molar mass ($kg.mol^{-1}$)
n	Matter amount (mol)
P	Pressure (Pa)
q	Specific heat quantity ($J.kg^{-1}$)
Q	Heat quantity (J)
R	Ideal gas law constant ($J.mol^{-1}.K^{-1}$)
R_p	Pressure ratio ($-$)
R_v	Volumetric expansion ratio ($-$)
s	Specific entropy ($J.kg^{-1}.K^{-1}$)
T	Temperature (K)
v	Specific volume ($m^3.kg^{-1}$)
V	Volume (m^3)
w	Specific work production ($J.kg^{-1}$)
W	Mechanical work (J)
x	Vapor quality ($-$)
X	Reaction advancement ($-$)

Greek letters

ε	Composite porosity ($-$)
η	Efficiency ($-$)
ν	Stoichiometric coefficient ($-$)
ρ	Density ($kg.m^{-3}$)
τ	Ratio ($-$)

Superscripts

0	Reference conditions

Subscripts

I	Energy-related
amb	Ambient level
an	Anhydrous reactive salt
C	Charging step
$cold$	Cold production level

$comp$	Composite reactive material
$cycled$	Involved in one complete cycle
D	Discharging step
dec	Decomposition reaction
ENG	Expanded Natural Graphite
eq	Thermodynamic equilibrium
$evap$	Evaporation
ex	Exergy-related
$high$	High pressure level
HTE	High Temperature Equilibrium
H/HTS	High Temperature reactor/Salt
hot	Heat source level
HX	Heat exchange
$HX1$	Liquid/liquid or liquid/vapor heat exchange
$HX2$	Vapor/vapor heat exchange
in	Input (energy or exergy)
is	Isentropic
low	Low pressure level
LTE	Low Temperature Equilibrium
L/LTS	Low Temperature reactor/Salt
$LV-eq$	Liquid/vapor phase change equilibrium
m	Mid-level
max	Maximal value
met	Metal of the chemical reactor
min	Minimal value
$NH3$	Ammonia
nom	Nominal value
p	Poor (reactive salt after decomposition)
$perfect$	'Perfect' case
$porous$	Porous volume
r	Rich (reactive salt after synthesis)
$r-eq$	Chemical reaction equilibrium
$salt$	Reactive salt (HTS or LTS)
sup	Superheat
w	Work production

1. Introduction and state-of-the-art review

The current energy context makes managing the time-variability and diversity of energy forms a key issue. The energy mix is increasingly integrating various renewable sources, but waste heat from industry is also still a significant energy pool that remains underexploited: for instance, the annual surplus heat from industrial processes in the UK is estimated at between 10 and 40 TWh [1]. Both sources are low-carbon, but they are also time-variable, and their low temperature levels make conversion into power more difficult. Energy demand also varies widely over time, not only in power levels but also in form (e.g. electricity, cooling or heating).

The challenge is to ensure the optimal use of these various low-carbon energy sources to meet the wider form and amount of demand and to cope with the time-variability of both supply and needs. Roskilly et al. [2] recently identified several systems as promising means of improving thermal energy management in industry, buildings and transport sectors. Focusing on energy resources, Ling-Chin et al. [3] estimated the temperature ranges of various industrial low-grade waste heat sources (e.g. petrochemical, iron, paper, cement and food sectors). These studies show that the most suitable existing waste-to-value systems for low-grade heat are currently monofunctional processes, such as liquid/gas absorption or solid/gas thermochemical refrigeration cycles, Organic Rankine Cycles (ORC) or Kalina cycles.

Developing cogeneration cycles by combining two of these monofunctional processes is therefore a promising way to improve the recovery of low-grade heat. Such cycles are called hybrid thermodynamic cycles. They pool the common components (e.g. evaporator, condenser) and working fluid of each cycle to build a single cycle that integrates the useful features of both. For example, hybridizing a sorption refrigeration cycle with an ORC consists in integrating an expansion device in the sorption cycle to provide additional power production. Hybrid thermodynamic cycles are increasingly gaining attention in research aiming to improve energy management by means of novel multi-purpose systems. However, the concept is still only emerging.

Regarding hybrid cycles involving a sorption process for combined power and cooling applications, Ziegler et al. [4] developed a broad approach inspired by the Honigmann system that covers the various types of sorption processes (liquid/gas absorption, solid/gas adsorption and chemical reaction). They proposed a generalized cycle configuration with five main components (condenser, evaporator, desorber, ab- or adsorber and expander), enabling flexible inputs (heat or power) and outputs (power or cold). A theoretical study was carried out on a power cycle using liquid/gas absorption (with $LiBr/H_2O$ as the working pair): for a heat source temperature of 120°C and a heat release temperature of 69°C, energy efficiency reached 0.10 and exergy efficiency was 0.41 (computed with the data available in [4]). Focusing on the hybridization of a liquid/gas absorption refrigeration cycle with an ORC, one of the first cycle layouts was proposed by Goswami et al. [5]. Involving ammonia-water mixture as the working fluid, their hybrid cycle used a heat source at 127 °C to provide both mechanical power and cold at -10 °C. The main output was mechanical power (around 74 % of the overall cogeneration output) and energy and exergy efficiencies were 0.24 and 0.59, respectively. Further investigations on this cycle showed that the most significant source of irreversibility was the non-isentropic expansion process in the turbine, and an experimental setup successfully operated to demonstrate the feasibility of this combined power and cooling cycle [6]. Later, Ayou et al. [7] overviewed the existing hybrid cycles involving liquid/gas absorption process for power and cold cogeneration. They concluded that power is usually the main output and that energy efficiencies range from 0.12 to 0.45 while exergy efficiencies range from 0.35 to 0.59, according to operating temperatures and system designs.

Nadeem et al. [8] analyzed the time-variability of energy resources and consumption, they concluded that there is a need to develop new topologies of storage systems providing higher energy storage densities and lower costs for a given storage capacity to be more competitive. In this context, the development of power and cold cogeneration cycles offering an energy storage feature is a promising new route towards improving the conversion of intermittent low-grade heat. The above-described hybrid cycles involving a liquid/gas absorption process run in continuous-mode operation (the solution circulates continuously between the gas absorber and desorber) and so cannot integrate storage of the heat input. However, hybrid cycles involving a solid/gas sorption process (adsorption or thermochemical) run in discontinuous-mode operation (as the solid adsorbent or reactant is usually implemented in a fixed-bed vessel) and so can address this storage issue. Among them, systems based on a solid/gas thermochemical process have been far less investigated, although their energy storage densities can reach more than 500 kWh/m^3 [9]. The following state-of-the-art review focuses on such hybrid thermochemical cycles using ammonia as reactive gas, as it offers a wide variety of available solid reactants, and thus a wide range of feasible temperature and pressure conditions.

One of the first hybrid thermochemical cycles for power and cold cogeneration was proposed and investigated by Wang et al. [10]. Using two solid reactants implemented in two separate fixed-bed reactors, their cycle (called resorption cycle) operated under heat source temperatures in the range 100-400 °C. Heat sink temperature was 30 °C and cold production temperature was in the range -10-10 °C. The thermodynamic study

showed that Coefficient Of Performance (COP) and exergy efficiency could reach 0.77 and 0.90, respectively. Later, this research team investigated a lab-scale prototype involving two sets of thermochemical cycles working out-of-phase for continuous cold production and a scroll expander for power generation [11]. Heat source and heat sink temperatures were set at 125 °C and 30 °C, respectively. They found that ensuring a stable power output at the expander is a key technical challenge, because of the dramatically varying desorption rate in the reactor. Cold production temperature varied widely (the mean value was 10 °C), as well as power output (maximal power production was 490 W). Bao et al. [12] proposed a theoretical study on the dynamic behavior of such hybrid thermochemical cycle. Based on the dynamic modelling of each component of the system, this work further highlighted the strong coupling between reactor and expansion device: indeed, power output was only around one third of the expected value (computed with the individual expander model under the same conditions), because of the mutual constraint between these two components when they link in series. Another technical limitation of hybrid thermochemical cycles is ammonia expansion (wet fluid). To overcome this limitation, Bao et al. [13] integrated a reheating process upstream of the expander, thus increasing the expansion ratio without damaging the expansion device. An optimization process was carried out to maximize work output, and the cycle was able to provide cooling output between -28 and 9°C. Under heat source temperatures in the range 70-200°C and a heat sink temperature at 25°C, cycle energy efficiency ranged from 0.06 to 0.24 and cycle exergy efficiency ranged from 0.50 to 0.85. Bao et al. [14] also designed a cycle using ultra-low-grade heat (source temperature in the range 30–100°C) to generate power only. This cycle used a compressor to assist the decomposition reaction at very low heat source temperatures, and with a heat sink temperature of 30°C, its thermodynamic performances ranged from 0.47 to 0.62 for energy efficiency and from 0.71 to 0.90 for exergy efficiency, depending on the heat source temperature. Later, they proposed a comparison of pumpless ORC against resorption power cycles [15]. They evaluated work output per unit mass of working fluid as 100–550 kJ/kg for the resorption cycle against 10–100 kJ/kg for pumpless ORC. The reason for this difference was the low molecular weight of ammonia compared with the organic fluid used in ORC. Using a low-grade heat source between 60°C and 180°C and a heat sink temperature of 30°C, energy efficiency ranged from 0.08 to 0.25 for pumpless ORC but was much lower (0.06–0.17) for the resorption cycle. Bao et al. [16] also investigated a multiple expansion resorption cycle implementing 2-4 expansion stages that used a heat source between 30°C and 150°C and a heat sink temperature of 25°C. It achieved a slightly higher work output per unit mass of working fluid (100–600 kJ/kg) but similar energy efficiencies (0.06–0.15) to those obtained in [15]. One of the main conclusions of this work was the need to balance the choice between more total work output (more expansions) and a more compact system with higher average output per expansion device. Lu et al. [17] designed a system involving two resorption cycles operating in phase opposition to provide a full-power output. Recovering low-grade heat from two heat sources at 180–200°C and 80–90°C, it enabled continuous operation. The reactive ammonia salts $MnCl_2$ and $SrCl_2$ were chosen as working pairs, and the system led to a thermal efficiency of about 0.11 in each mode. Their detailed dynamic study [18] stressed the importance of the expander-chemical reactor coupling and the need to manage the coupling pressure to firmly control power output. Lu et al. went on to investigate a similar system [19,20] with the aim of providing continuous power and cooling outputs instead of power only. Heat source temperature was in the range 100-200°C and heat sink temperature was set at 20°C. Mass and heat recovery processes were integrated to further improve system performance. Adding a buffer upstream of the expander was found to deliver a stable pressure supply (and therefore a stable power output), despite the dramatically varying reaction rate. For the most promising reactive salts, cogeneration energy and exergy efficiencies ranged from 0.64 to 0.75 and from 0.45 to 0.58, respectively. In the experimental study [21], they assessed the viability of using a scroll expander for power generation: under similar working conditions (heat source and heat sink temperatures), the expander was tested with success, and its isentropic efficiency was estimated to be around 0.6. Jiang et al. [22] studied another experimental setup of a resorption power and cold cogeneration cycle and their work highlighted the technical difficulty of achieving a stable power output due to strong coupling between chemical reaction kinetics and the dynamics of the expansion process. They went on to propose an improvement of resorption cycles using a novel composite sorbent [23], and obtained energy efficiencies in the range 0.11–0.14 and exergy efficiencies from 0.62 to 0.81, with a heat source temperature between 80°C and 110°C and a heat sink (ambient temperature) at 30 °C. Finally, their recent work [24] highlighted how hybrid thermochemical cycles hold promising potential for low-grade heat utilization: using heat source temperatures in the range 200–360°C and a heat sink temperature of 35°C, their novel resorption cycle integrating internal heat recovery provided a refrigeration effect at 0°C with a COP of 1.3 and exergy efficiencies between 0.41 and 0.74.

This state-of-the-art review finds promising thermodynamic performances of existing hybrid thermochemical cycles, with energy and exergy efficiencies that can reach 0.75 and 0.90, respectively. However, most studies to date have been based on optimistic assumptions, especially about temperature pinches and irreversibilities in the expansion processes. Moreover, only a few reactive materials have been considered.

The aim of this study is to provide a systemized analysis of several novel hybrid thermochemical cycles using ammonia as reactive gas for a wide set of solid reactive materials (103 reactive salts), using realistic thermodynamic assumptions. In this analysis, the heat source temperatures lie under $T_{hot,max} = 250$ °C. The heat sources can, for example, be solar sources or industrial waste heat. Such systems could be used in places where electricity and cold production are needed in varying proportions (typically food stores or industries) or in mobile applications, for example refrigerated goods delivery in urban areas. Eco-industrial parks are also an example of promising prospect for the implementation of such hybrid cycles, because they could combine low temperature waste heat with power and cold demand. The storage feature of the proposed systems allows to cope with the time-variability of low-grade heat resource.

This paper brings innovation to the current body of knowledge in the field of hybrid thermodynamic cycles by introducing novel hybrid thermochemical cycles, which despite their attractive storage capability have been less thoroughly investigated than other hybrid cycles. Several hybrid thermochemical cycles were recently investigated to achieve power and cold cogeneration, with cold production dominant [25]. Here we investigate two novel cogeneration modes whose dominant output is power generation, to address the increasing demand for power. Moreover, for each mode, an innovative autothermal working step (operating without any external heat supply) is designed and investigated. Compared to previous studies, this paper also develops a more comprehensive thermodynamic study: regarding the performance assessment of the cycles, a set of four relevant criteria is introduced to provide a complete overview of energy and exergy performances. Regarding the choice of solid reactants, a broad panel of reactants (103 reactive salts) is reviewed. Such extensive approach allows to identify the most promising cycles and reactants, as a basis for future experimental investigations.

First we present the general working principle of the proposed hybrid thermochemical cycles, which is characterized by an autothermal working step. We then detail the two operating modes (**discharge** power generation mode and **combined charge and discharge** power generation mode) and present the framework of our thermodynamic study (assumptions, model and methodology). We go on to provide a deeper analysis of the behavior of the autothermal power generation step, and the results of this thermodynamic study, including operating conditions and performances, are then detailed in the two sections relating to each mode. Finally, these results are brought together and discussed in a sensitivity study on some key variables and a comparison of the operating conditions and performances of all the investigated hybrid cycles. We conclude by discussing the most appropriate applications of each cycle, together with outlooks and perspectives.

2. Combined power and cooling hybrid thermochemical cycle with dominant power output

The proposed hybrid cycle involves three components: two chemical reactors (the thermochemical part of the cycle) and one expander (the power part of the cycle). These components are depicted in *Fig. 1*. This configuration of hybrid cycle involving two chemical reactors is called *resorption* cycle. The thermochemical process is based on reversible solid/gas chemical reactions and each reaction is implemented in a fixed-bed reactor. Therefore, hybrid cycle operation is split into two steps: a charging step (the upper part of *Fig. 1*) and a discharging step (lower part of *Fig. 1*). Thanks to this two-step operation, heat supply and outputs (power and/or cold production) can be time-shifted, which provides the storage feature of the cycle.

Each reactor is filled with a solid composite material, which is a porous medium made up of a reactive ammonia salt mixed with Expanded Natural Graphite (ENG) to enhance heat transfer. The cycle involves two different reactive salts:

- In the left-hand reactor of *Fig. 1*, the reactive salt is called Low-Temperature Salt (LTS) because this reactor operates at a lower temperature than the other one.
- In the right-hand reactor of *Fig. 1*, the reactive salt is called High-Temperature Salt (HTS) because of its higher working temperatures.

For each reactor, a monovariant thermodynamic equilibrium (solid/gas chemical reaction equilibrium set by the thermochemical properties of the corresponding reactive salt) provides a relationship between its working pressure and temperature. The whole cycle is therefore characterized by two independent thermodynamic equilibria: the Low-Temperature Equilibrium (LTE) associated with the left-hand reactor of *Fig. 1* (and set by the LTS), and the High-Temperature Equilibrium (HTE) associated with the right-hand reactor of *Fig. 1* (and set by the HTS).

In each step, the two reactors exchange heat with external exchangers and vapor between them: a decomposition reaction (endothermal process generating vapor) takes place in one reactor, while a synthesis reaction (exothermal process consuming vapor) occurs in the other reactor. The expander can be actuated on the vapor flow between these two components to generate power.

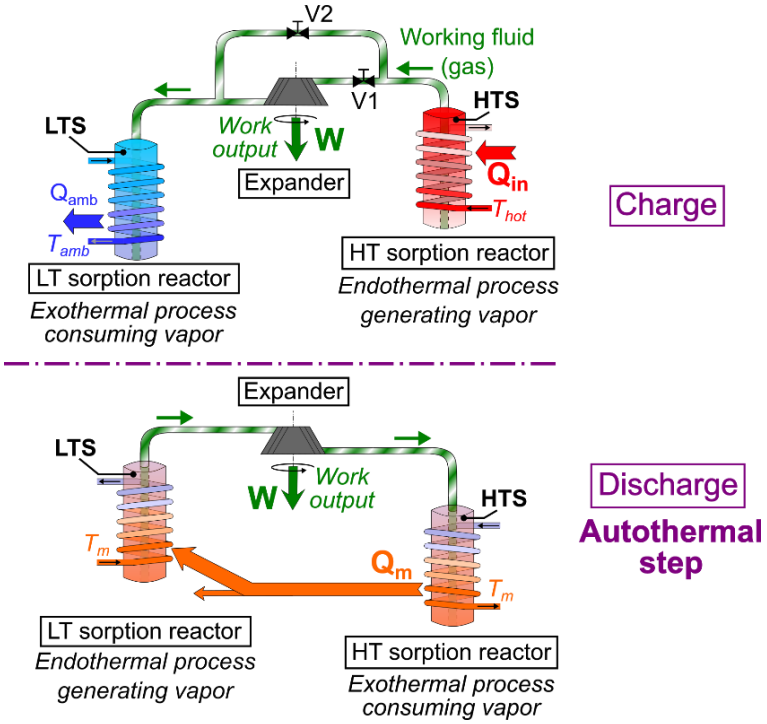

Fig. 1 – Resorption hybrid thermochemical cycle for power and cold cogeneration with dominant power output: operating principle. Valves V1 and V2 are not displayed in the discharging step because the expander is always actuated in this step.
(i) Discharge power generation mode: valve V1 is closed and valve V2 is open (details in Fig. 2 and Fig. 4).
(ii) Combined charge and discharge power generation mode: valve V1 is open and valve V2 is closed (details in Fig. 3 and Fig. 5).

2.1. Operation of the hybrid cycle

The hybrid cycle operates as follows:

- In the charging step (upper part of *Fig. 1*), input heat Q_{in} is supplied by the external source to trigger the endothermal decomposition reaction (in the right-hand reactor), which generates vapor. Downstream, the exothermal synthesis reaction (in the left-hand reactor) consumes the inflowing vapor and releases heat Q_{amb} at ambient temperature. Valves V1 and V2 serve to actuate the expander using the vapor flow to provide power if desired.
- In the discharging step (lower part of *Fig. 1*), the roles of each component are reversed. The respective endo- and exothermal effects of the decomposition reaction (vapor generation) and the synthesis reaction (vapor consumption) are connected in order to achieve an autothermal step: the heat Q_m released by the synthesis reaction is recovered to trigger the endothermal decomposition reaction. An expander is actuated on the vapor flow between the (upstream) decomposition reactor and the (downstream) synthesis reactor to generate power. Finally, according to outlet pressure of the expander, the vapor flow can reach low temperatures, thus providing an additional cold production.

Finally, from the general layout of the hybrid thermochemical cycle presented in *Fig. 1*, several operating modes can be defined according to how the expansion devices are actuated:

(i) **Discharge** power generation mode if power output occurs during the autothermal discharging step, while the charging step is isobaric.

(ii) **Combined charge and discharge** power generation mode if power output occurs in both charging and discharging steps.

The following analyses are arranged along these modes: first we discuss the **discharge** power generation mode (see Section 4), then we deal with the **combined charge and discharge** power generation mode (Section 5) in a symmetrical manner.

2.2. Discharge power generation mode

The pattern of the thermodynamic cycle in **discharge** power generation mode is given on a Clausius-Clapeyron diagram in *Fig. 2*. This diagram highlights the two distinct operating steps and the corresponding temperature and pressure levels, together with the energy flows (heat and mechanical work).

Once again, operation of this hybrid cycle is based on two monovariant thermodynamic equilibria: the LTE and the HTE, which are plotted in *Fig. 2* (black straight lines). As mentioned above, pressures and temperatures in the left-hand reactor of *Fig. 1* are close to LTE conditions (points 10-11-12 and 13-1-2 in *Fig. 2*), while those in the right-hand reactor are close to HTE conditions (points 7-8-9 and 4-5-6 in *Fig. 2*). The cycle works discontinuously, which is what confers its intrinsic energy storage feature. Its two operating steps are detailed below:

- The charging step (pink path, left side of *Fig. 2*) is an isobaric step. The input thermal energy (low-grade heat Q_{in}) is used to bring the HTS out of thermodynamic equilibrium (HTE), which triggers its endothermal decomposition and the generation of superheated ammonia vapor (points 7-8-9). Ammonia vapor then flows towards the synthesis reactor, where it is consumed by the exothermal synthesis reaction of the LTS (points 10-11-12). Synthesis heat (Q_{amb}) is released at the lowest available heat sink, i.e. at ambient temperature.
- The discharging step (green path, right side of *Fig. 2*) is a non-isobaric step. Coupling is implemented between the thermal effects of the decomposition reaction (vapor generation) and the synthesis reaction (vapor consumption): the HTS-synthesis heat Q_m, produced at points 4-5-6, first allows the LTS decomposition reaction to take place (points 13-1-2) and then superheats the generated ammonia vapor up to point 3. An expander is placed between points 3 and 3' to generate power, making use of the vapor flow between high-pressure and low-pressure reactors. Finally, expanded ammonia vapor flows towards the synthesis reactor where it reacts with the HTS (synthesis reaction: points 4-5-6).

Based on this diagram, we underline that:

- Three temperature levels define the heat source and sinks of the cycle, with $T_{amb} < T_m < T_{hot}$. Nevertheless, a fourth temperature level $T_{cold} < T_{amb}$ may be considered if the temperature at the expander outlet (point 3') is low enough to provide a refrigeration effect.
- Three pressure levels have to be considered to define both the isobaric charging step and the non-isobaric discharging step, i.e. P_C, $P_{low,D}$ and $P_{high,D}$. P_C is the pressure of the charging step, and $P_{low,D}$ and $P_{high,D}$ are respectively the low and high pressures of the discharging step. These pressure levels may be ordered differently from *Fig. 2* depending on T_m and on the superheat $(T_3 - T_1)$.
- Synthesis heat Q_m of the discharging step (orange arrows) is assumed to be high enough to ensure both vapor generation (transformation 13-1-2) and superheating (2-3) upstream of the expander, from which follows the autothermal behavior of the discharging step. Residual heat is released at temperature level T_m.

Finally, *Fig. 2* also specifies several temperature pinches:

- Temperature pinch ΔT_{HX} for heat exchange with a heat source or sink.
- Temperature deviation from the thermodynamic equilibrium line, ΔT_{eq}.

These parameters are required in real-world process operation, and they are detailed in the framework of the thermodynamic study in Section 3.1.

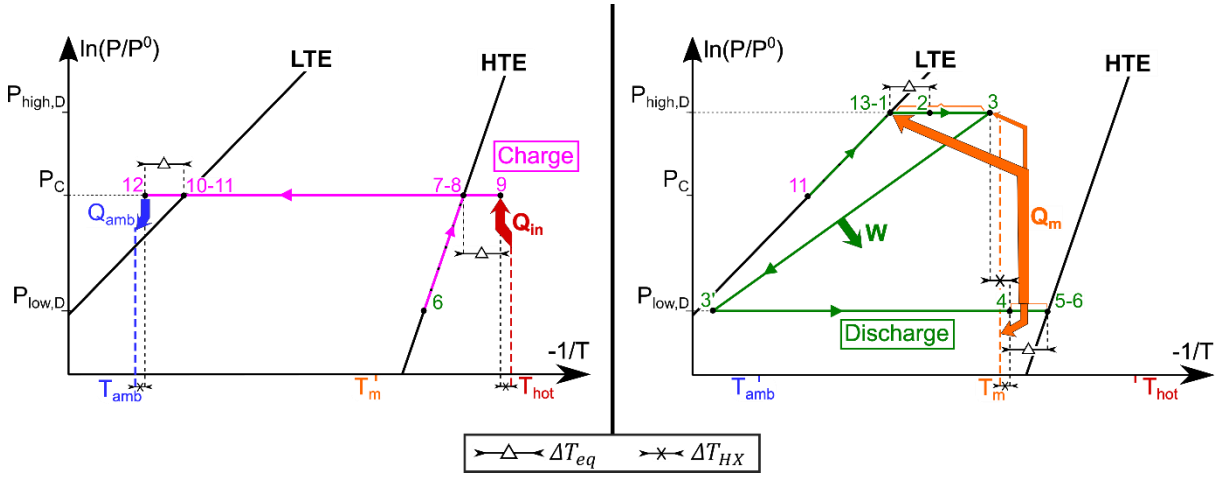

Fig. 2 – Discharge power generation mode of the hybrid thermochemical cycle: thermodynamic path in a Clausius-Clapeyron diagram (Left side: charging step. Right side: discharging step). For the sake of clarity, the switching step between charging and discharging steps is displayed in a simplified way (considering only points 6 and 11 on the equilibrium lines)

2.3. Combined charge and discharge power generation mode

Like *Fig. 2*, the pattern of the thermodynamic cycle in **combined charge and discharge** power generation mode is given on a Clausius-Clapeyron diagram in *Fig. 3*. This mode operates as follows:

- The charging step (pink path) is a non-isobaric step. As in Section 2.2, input heat Q_{in} enables the HTS decomposition reaction to take place (points 7-8-9). An expander is used to generate power from the ammonia vapor flow leaving the reactor (points 9-9'). The expanded vapor then flows towards the synthesis reactor where the LTS synthesis reaction takes place (points 10-11-12).
- The discharging step (green path) operates in the same way as in the discharge power generation mode (see Section 2.2).

The expansion device in the charging step is designed to increase the power production of this hybrid process. This has two main consequences:

- Concerning the temperature levels of the cycle, since the decomposition of the HTS takes place at a higher pressure ($P_8 = P_9 = P_{high,C}$) than previously, the regeneration temperature T_{hot} is higher than in discharge power generation mode.
- Concerning pressure levels, the system is characterized by four pressure levels instead of three: $P_{high,C}$ and $P_{low,C}$ for the non-isobaric charging step, and $P_{high,D}$ and $P_{low,D}$ for the non-isobaric discharging step. $P_{low,D}$ is the lowest pressure of the cycle; other pressures may be ordered differently from *Fig. 3* depending on T_m and on the superheat $(T_3 - T_1)$.

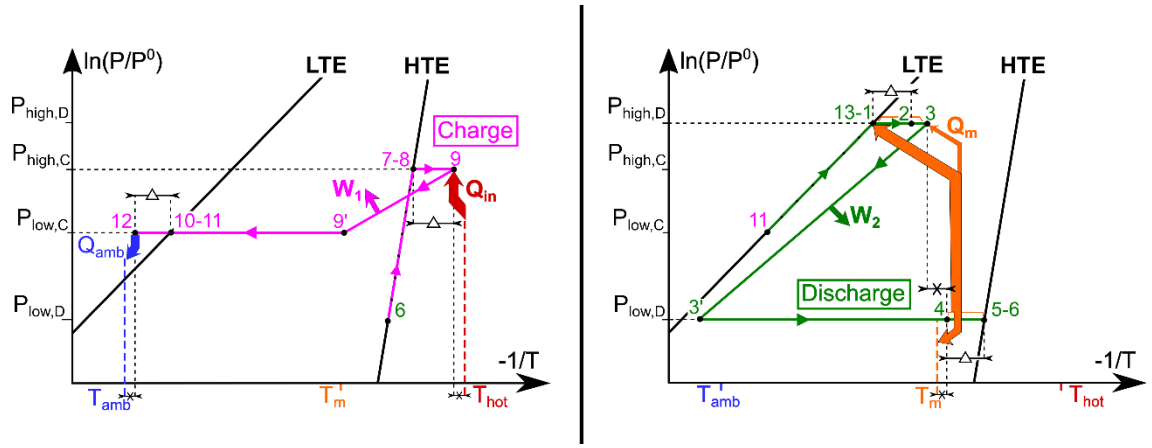

Fig. 3 – Combined charge and discharge power generation mode of the hybrid thermochemical cycle: thermodynamic path in a Clausius-Clapeyron diagram (Left side: charging step. Right side: discharging step). For the sake of clarity, the switching step between charging and discharging steps is displayed in a simplified way (considering only points 6 and 11 on the equilibrium lines). See Fig. 2 for caption details

2.4. The single sorption cycle: a change in the layout of the hybrid thermochemical cycle

The working principle described above applies to a combined power and cooling hybrid thermochemical cycle that uses two sorption reactors, and thus two solid reactive salts (LTS and HTS): such cycle is called a *resorption* cycle. However, this working principle can be extended to a special case where the low-temperature reactor (left-hand component in *Fig. 1*) is replaced by a reactive fluid condenser/evaporator, in which case the resulting cycle is called a *single sorption* cycle. This means that the left-hand component in *Fig. 1* contains ammonia (in gas and liquid phases) instead of LTS, and the LTE is the ammonia liquid/vapor phase change equilibrium instead of the LTS solid/gas chemical reaction equilibrium.

Therefore, for each operating mode (discharge and combined charge and discharge power generation modes), the LTE (and thus the left-hand component in *Fig. 1*) can be chosen in different ways: it can be either a solid/gas chemical reaction equilibrium (*resorption* cycle: the left-hand component in *Fig. 1* is a solid/gas chemical reactor filled with LTS) or a liquid/vapor phase change equilibrium (*single sorption* cycle: the left-hand component in *Fig. 1* is a reactive fluid condenser/evaporator).

Finally, the choice of LTE leaves room for two cycles in each operating mode, i.e. a *resorption* cycle (which is the most classical cycle in the literature) and a *single sorption* cycle.

The thermodynamic paths of single sorption cycles are plotted on schematic T-s diagrams in *Fig. 4* for the discharge power generation mode and *Fig. 5* for the combined charge and discharge power generation mode. In these diagrams, LTE is the ammonia liquid/vapor phase change equilibrium, while HTE is a solid/gas chemical reaction equilibrium. Consequently, the LTE curve gives the temperature and entropy of ammonia in saturated liquid (left) and saturated vapor (right) states, while the HTE curve gives the temperature and entropy of ammonia in adsorbed (left) and desorbed (right) states. This HTE curve is obtained by using thermochemical data on the solid reactant (HTS) together with suitable assumptions. Neveu et al. [26] detailed the method for building thermodynamic equilibrium curves of sorption reactions for ammonia salts in several thermodynamic diagrams.

Adding the T-s diagrams (*Figs. 4* and *5*) to the Clausius-Clapeyron diagrams (*Figs. 2* and 3) gives a more comprehensive picture of the cycle: *Figs. 2* and *3* fail to account for entropy variations of the working fluid during chemical reactions and phase changes (points 5-6, 7-8, 10-11 and 13-1), while T-s diagrams allow highlighting these variations.

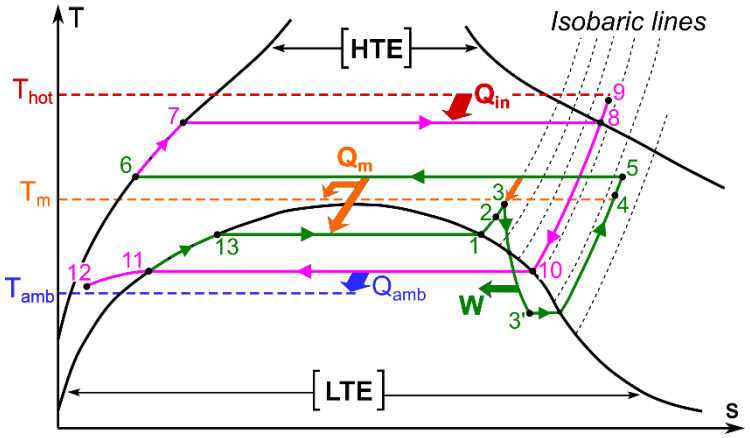

Fig. 4 – Discharge power generation mode of the hybrid thermochemical cycle (single sorption cycle): thermodynamic path in the T – s diagram of ammonia (see Fig. 2 for caption details)

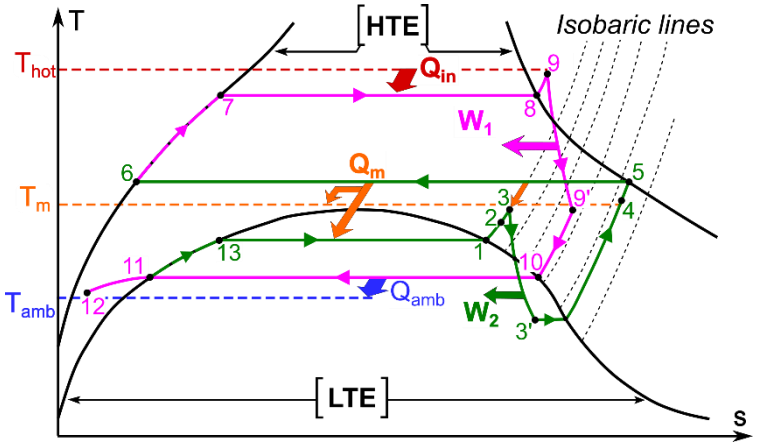

Fig. 5 – Combined charge and discharge power generation mode of the hybrid thermochemical cycle (single sorption cycle): thermodynamic path in the T – s diagram of ammonia (see Fig. 2 for caption details)

3. Thermodynamic analysis

A thermodynamic study is required to assess the energy and exergy performances of the proposed cycles and to identify the most promising cycle design (operating mode and configuration: resorption or single sorption) and reactive salts. This will help paving the way for future dynamic and experimental studies. To this end, a steady-state thermodynamic model based on energy balance equations has been developed. This section details the main assumptions and equations of this model and the framework of the thermodynamic study: operating conditions, methodology and performance criteria.

3.1. Model

For the thermodynamic study, the following assumptions are made:

- The system operates in steady state (though not realistic due to the highly dynamic chemical reaction process, this assumption allows an energy-related study as a first approach).
- Kinetic and potential energy variations are negligible in comparison with the enthalpy variations caused by thermal and chemical transformations in the components.
- Heat exchange with surroundings (except heat sources and sinks) are negligible for all components.
- Pressure drops are also negligible.
- Expansion of the working fluid in the expander is characterized by an isentropic efficiency, η_{is}.
- External and internal heat exchanges are modeled considering the following temperature pinches:
  - For (liquid/liquid) or (liquid/vapor) heat exchange: ΔT_{HX1}.
  - For (vapor/vapor) heat exchange: ΔT_{HX2}.
  - For the deviation from thermodynamic equilibrium lines (LTE and HTE): ΔT_{eq}.
- The reference temperature for exergy calculations is set at $T^0 = T_{amb}$.

As indicated in Section 2, the thermodynamic path of the hybrid cycle is bounded by two thermodynamic equilibrium curves (LTE and HTE: straight lines in *Fig. 2* and *Fig. 3*, bell-shaped curves in *Fig. 4* and *Fig. 5*). Each of these thermodynamic equilibria is monovariant, and so can be expressed as $P = \Pi(T)$. For a solid/gas chemical reaction equilibrium, we get:

$$ln\left(\frac{P}{P^0}\right) = -\frac{\Delta_r H^0}{R.T} + \frac{\Delta_r S^0}{R} \quad \textbf{(1a)}$$

The thermodynamic states of the fluid at each point of the cycle are computed according to the transformations described in Sections 2.2 and 2.3 (and in *Figs. 2-5*). Once the thermodynamic path is determined, energy-related quantities (supplied and released heat, mechanical work produced) are computed, using the following energy balance equations:

$$\mathrm{Q}_{in} = n_{NH3,cycled}.\Delta_r H(T_7, P_7) + \left[V_{met,H}.\rho_{met}.c_{met} + n_{HTS}.\bar{C}_{HTS}\right].(T_9 - T_4) \quad \textbf{(2)}$$

$$\mathrm{Q}_{cold} = m_{NH3,cycled}.(h_{NH3}(T_{cold} - \Delta T_{HX2}, P_4) - h_{3'}) \quad \textbf{if} \quad \boldsymbol{T_{3'} < T_{cold} - \Delta T_{HX2}} \quad \textbf{(3)}$$

$$\mathrm{Q}_m = n_{NH3,cycled}.\Delta_r H(T_5, P_5) - m_{NH3,cycled}.c_{NH3}.(T_m - T_{amb}) \quad \textbf{(4)}$$

$$\mathrm{Q}_{sup} = m_{NH3,cycled}.(h_3 - h_2) \quad \textbf{(5)}$$

$$\mathrm{Q}_{dec,L} = n_{NH3,cycled}.\Delta_r H(T_1, P_1) + \left[V_{met,L}.\rho_{met}.c_{met} + n_{LTS}.\bar{C}_{LTS}\right].(T_2 - T_{12}) \quad \textbf{(6a)}$$

For **discharge** power generation mode (see *Fig. 2* and *Fig. 4*):

$$\mathrm{W} = m_{NH3,cycled}.(h_3 - h_{3'}) \quad \textbf{(7)}$$

For **combined charge and discharge** power generation mode (see *Fig. 3* and *Fig. 5*):

$$\mathrm{W} = m_{NH3,cycled}.(h_3 - h_{3'}) + m_{NH3,cycled}.(h_9 - h_{9'}) \quad \textbf{(8)}$$

Here:

$$\bar{C}_{HTS} = X_{max}.C_{HTS,r} + (1 - X_{max}).C_{HTS,p} \quad \textbf{(9)}$$

and $$\bar{C}_{LTS} = X_{max}.C_{LTS,r} + (1 - X_{max}).C_{LTS,p} \quad \textbf{(10)}$$

In Eqs. **(9)** and **(10)**, X_{max} is the maximum value of the reaction advancement X such that:

$$0 < X_{min} < X_{max} < 1 \quad \textbf{(11)}$$

and $$X_{min} = 1 - X_{max} \quad \textbf{(12)}$$

$\bar{C}_{HTS}$ and $\bar{C}_{LTS}$ are the molar heat capacities of solid reactive salts implemented in the High Temperature (Eq. **(9)**) and Low Temperature (Eq. **(10)**) reactors after the synthesis reaction, respectively. For more details on the computation of $C_{HTS,r}$, $C_{HTS,p}$, $C_{LTS,r}$ and $C_{LTS,p}$, see Appendix A.

The feasibility of the autothermal discharging step is then checked by comparing the heat released during HTS synthesis reaction, Q_m, with the heat required to ensure both heating of the Low Temperature reactor, vapor generation (from the LTS decomposition reaction) and superheating of this generated vapor: the condition $Q_m > Q_{dec,L} + Q_{sup}$ must be met to ensure the viability of the autothermal behavior.

Regarding the model assumptions, an isentropic efficiency (η_{is}) is defined for expanders. It is the ratio of the real enthalpy variation between expander outlet and inlet and the enthalpy variation if the expansion were isentropic. For example (see *Figs. 2-5*):

$$\eta_{is} = (h_{3'} - h_3)/(h_{3',is} - h_3) \quad \textbf{(13)}$$

To define the characteristics of chemical reactors, the following parameters and equations are also considered:

- The variation range of reaction advancement, $\Delta X = X_{max} - X_{min}$, such that:

$$n_{NH3,cycled} = v_{salt}.\Delta X.n_{salt} \quad \textbf{(14)}$$

- The ratio of metal to reactive composite volume, τ_{met}, such that:
$$V_{met} = \tau_{met}.V_{comp} \quad \textbf{(15)}$$
This parameter is related to the thermochemical reactor configuration; it is included in the sensible heat terms of Eq. **(2)** and **(6a)**.

- The porosity ε of composite bed implementing the reactive salts in reactors, which is set at 0.7. This parameter is such that $V_{porous} = \varepsilon.V_{comp}$ and $V_{salt} + V_{ENG} = (1-\varepsilon).V_{comp}$.

Based on experience with ORC and refrigeration thermochemical machines, the following values have been set for the simulation parameters: $\eta_{is} = 0.8$, $\Delta X = 0.8$, $\tau_{met} = 0.1$, $\Delta T_{HX1} = 5$ K, $\Delta T_{HX2} = 10$ K and $\Delta T_{eq} = 20$ K. A sensitivity analysis has been carried out to assess the effects of changing the values of these parameters on simulation results: this study is detailed later (see Section 6.1). A simulation based on a 'perfect' set of parameters values (η_{is}, ΔX, τ_{met}, ΔT_{HX1}, ΔT_{HX2} and ΔT_{eq}) has also been achieved. The results of this simulation, detailed in Appendix B, aim to provide another basis for comparison with existing studies, given that they usually rely on optimistic assumptions (especially about temperature pinches and irreversibilities in the expansion processes).

- Single sorption cycles: we note that single sorption cycles are based on ammonia liquid-vapor equilibrium as the LTE, instead of a solid/gas chemical reaction equilibrium (see Section 2.4). In this case, the temperature deviation from LTE line is set at $\Delta T_{LV\text{-}eq} = 0$ K while the temperature deviation from HTE line is $\Delta T_{r\text{-}eq} = 20$ K, because liquid/vapor phase change is usually not rate-limiting, unlike solid/gas chemical reaction. Moreover, the monovariant LTE Eq. **(1a)** is replaced by:

$$ln\left(\frac{P}{P^0}\right) = -\frac{L_{vap}}{R.T} + \frac{\Delta S_{vap}}{R} \quad \textbf{(1b)}$$

, and the energy balance equation **(6a)** is replaced by:

$$Q_{evap} = n_{NH3,cycled}.L_{vap}(T_1) + m_{NH3,cycled}.c_{NH3}.(T_2 - T_{12}) \quad \textbf{(6b)}$$

Finally, the condition $Q_m > Q_{dec,L} + Q_{sup}$ is replaced by: $Q_m > Q_{evap} + Q_{sup}$ (to ensure the feasibility of the autothermal behavior).

3.2. Operating conditions and technological boundary values

The operating temperatures considered for this study are listed below:

- The ambient temperature (heat sink temperature, for the release of LTS synthesis or condensation heat) is set at $T_{amb} = 20$°C.
- The heat source temperature T_{hot} is not fixed, but instead deduced from the computation of thermodynamic states of the working fluid at key points of the cycle (as described in Section 3.1). However, a boundary value is set ($T_{hot,max} = 250$°C) to meet the target of using low-grade heat.
- Due to the expansion process, the temperature at the outlet of the expander (point 3' on *Figs. 2-5*) may be lower than ambient. Consequently, a cold production temperature $T_{cold} = 0$°C is set for the case where a refrigeration effect is achieved.

Several boundary values are also defined to address technical limitations:

- The ammonia pressure is bounded by $P_{min} = 0.1$ bar (to avoid mass transfer limitations in the reactive bed) and $P_{max} = 30$ bar.
- A minimal vapor quality $x_{min} = 0.8$ is required at the outlet of the expanders (to avoid damaging them).
- A maximal volumetric ratio $R_{v,max} = 10$ is assumed for expanders. In accordance with *Figs. 2-5* (in discharging step), the volumetric expansion ratio is defined by:
$$R_v = v_{3'}/v_3 \quad \textbf{(16)}$$

3.3. Methodology and performance criteria

The purpose of this study is to investigate the potential of the hybrid cycles described in Section 2 for different reactive salts. For each cycle, the Low Temperature Equilibrium is fixed:

- In the case of a resorption cycle, LTE is a solid/gas chemical reaction equilibrium using $BaCl_2$ (8/0)NH_3 as solid reactive salt (LTS). In addition to being a well-known reactant (already used in some commercial refrigeration machines), it shows low equilibrium temperatures, which offers a large expansion stage between points 3 and 3' (due to the large gap between LTE and HTE curves, see *Figs. 2-5*).

- In the case of a single sorption cycle, LTE is the liquid/vapor phase change equilibrium of ammonia.

Given that the system operates in steady state, this is an energy-related study. For each cycle, a work output $W = 1$ kWh is assumed. A database containing thermochemical data for 103 reactive salts (reaction enthalpy $\Delta_r H^0$ and reaction entropy $\Delta_r S^0$) is used. These salts are mainly metallic chlorides, bromides and iodides, such as $SrCl_2$, $MnCl_2$, $CaBr_2$, or SrI_2. The thermochemical properties in this database come from values collected and computed by Touzain [27] and from CNRS-PROMES research. The calculation process, using EES software [28], is based on screening all the reactive salts of this database: for each HTS,

- The thermodynamic path of the cycle (temperatures, pressures, specific enthalpies and entropies at key points of the cycle) is computed.
- The relevant extensive quantities are deduced (especially the cycled mass of working fluid $m_{NH3,cycled}$ from Eq. **(7)** or **(8)**, and then energy quantities from Eqs. **(2)** to **(6)**), as well as heat source temperature T_{hot}.

To identify the most promising cycles and the best reactive salts for each cycle configuration, several performance criteria have to be defined. The main features of the investigated systems are power production and energy storage; however, an additional cold production is considered in this thermodynamic study. The performance criteria used for this analysis are thus based on cogeneration system criteria:

- Energy efficiency,

$$\eta_I = \frac{W+Q_{cold}}{Q_{in}} \quad \textbf{(17)}$$

- Exergy efficiency,

$$\eta_{ex} = \frac{W+Ex_{cold}}{Ex_{in}} \quad \textbf{(18)}$$

- Specific work output,

$$w = \frac{W}{m_{NH3,cycled}} \quad \textbf{(19)}$$

- Specific exergy output,

$$w + ex_{cold} = \frac{W+Ex_{cold}}{m_{NH3,cycled}} \quad \textbf{(20)}$$

with $$Ex_{in} = Q_{in}.\left(1 - \frac{T^0}{T_{hot}}\right) \quad \textbf{(21)}$$

and $$Ex_{cold} = Q_{cold}.\left(\frac{T^0}{T_{cold}} - 1\right) \quad \textbf{(22)}$$

Firstly, η_I (Eq. **(17)**) is a well-known dimensionless criterion, widely used in thermodynamic analyses to assess the ability of a system to efficiently convert an input energy into useful energies. Although useful in an energy-related approach, it does not account for the "quality" of energy inputs and outputs, i.e. their exergy content (which quantifies their ability to generate mechanical work). The second dimensionless criterion (η_{ex}, Eq. **(18)**) addresses this issue by integrating the effect of temperature levels T_{hot} and T_{cold} on the exergy content of Q_{in} and Q_{cold}, respectively: Eq. **(21)** and **(22)**.

The specific quantities w and $w+ex_{cold}$ (Eq. **(19)** and **(20)**) are expressed relative to the cycled mass of working fluid (ammonia), providing a quantified overview of performance. We note that in discharge power generation mode (where useful effects are generated only during the discharging step), these two criteria are exergy storage densities, which allows a fair comparison with other thermal energy storage systems.

For each studied cycle and each technical layout (i.e. using 1, 2 or 3 expansion stages, to fulfil the technological constraint $R_v < R_{v,max}$), the 10 highest values (corresponding to 10 HTSs) are retained for each of these performance criteria. At the end of this process, about 30–50 HTSs are selected. All performance results for the selected salts are collected in Sections 4 and 5 for the two operating modes.

Finally, another key variable is used to assess the performance of the investigated cogeneration cycles: the power production ratio, defined in Eq. **(23)**.

$$\tau_w = \frac{W}{W+Q_{cold}} \quad \textbf{(23)}$$

This ratio enables us to identify the most relevant application of the system (cycle and HTS), because it gives the portioning between the two useful effects (power and cold production).

3.4. Analysis of the autothermal discharging step

The operating pressures of classical thermochemical cycle (for heat storage or cold production) are set by LTE and HTE curves and by heat source and heat sink temperatures. However, when the cycle includes an autothermal step, the synthesis temperature of this step (T_m) is an operative degree of freedom of the process. This section explains how the main temperature and pressure levels of the autothermal discharging step (points 13 to 6, green path in *Figs. 2-5*) are determined, depending on the chosen LTE and HTE. We note that for clarity, all temperature pinches (heat exchange with heat source and sink, deviation from thermodynamic equilibrium) are assumed to be zero for this analysis.

Unlike the charging step, which is characterized by two temperature levels (heat sink T_{amb} and heat source T_{hot}), the autothermal discharging step is characterized only by the HTS synthesis temperature, T_m, which results from the operating pressure of the reactor $P_{low,D}$: $T_m = T_{eq,HTE}(P_{low,D})$. As detailed in Section 2.2, in the autothermal step, the HTS synthesis reaction heat is used to drive LTS decomposition reaction and superheating of the working fluid, the excess heat being released at ambient sink. Consequently, the operation of this step requires:

(i) A HTS synthesis temperature equal to or higher than the LTS decomposition temperature (to ensure that heat can be transferred from HT reactor to LT reactor):
$T_m \geq T_{eq,LTE}(P_{high,D})$, thus $P_{eq,LTE}(T_m) \geq P_{high,D}$.

(ii) A HTS synthesis temperature equal to or higher than the ambient temperature (to enable the release of excess synthesis heat at ambient sink):
$T_m \geq T_{amb}$, thus $P_{low,D} \geq P_{eq,HTE}(T_{amb})$.

(iii) A LTS decomposition pressure higher than the operating pressure of the HTS synthesis reactor (to insert an expansion stage between LT and HT reactors):
$P_{high,D} \geq P_{low,D}$.

Also, due to technical limitations (described in Section 3.2):

(iv) The operating pressure of the HTS synthesis reactor ($P_{low,D}$) must be higher than P_{min}:
$P_{low,D} \geq P_{min}$, thus $T_m \geq T_{eq,HTE}(P_{min})$.

(v) The operating pressure of the LTS decomposition reactor ($P_{high,D}$) must be lower than P_{max}:
$P_{high,D} \leq P_{max}$.

Fig. 6 describes how the operating conditions of the autothermal step are determined, considering these 5 operating constraints. To illustrate this determination process, which depends on the working pair (LTS/HTS), three different reactive salts are used: High Temperature Salts HTS_1 (red line: HTE_1), HTS_2 (green line: HTE_2) and HTS_3 (blue line: HTE_3). In connection with *Figs. 2-5*, we note that points A_1, A_2 and A_3 are equivalent to points 13-1 (LTS decomposition reaction), while points B_1, B_2 and B_3 are equivalent to points 5-6 (HTS synthesis). A two-stage process sets the main temperature and pressure levels of the autothermal step:

- As a first step, the HTS synthesis temperature T_m (operative degree of freedom) is assigned a value in the range complying with the constraints (ii) and (iv). This is highlighted by the thick line on x-axis.
- As a second step, a constrained maximization process is carried out. Specific work output w is the objective function, and high pressure $P_{high,D}$ is the optimization variable. The thick segment on LTE line shows where point A can be placed, accounting for constraints (i), (iii) and (v).

For the three reactive salts, different boundary values are reached:

- For HTS_1, T_m is constrained by (ii) ($T_{m,1} = T_{amb}$).
- For HTS_2, $P_{low,D}$ is constrained by (iv) ($P_{low,D,2} = P_{min}$).
- For HTS_3, $P_{high,D}$ is constrained by (v) ($P_{high,D,3} = P_{max}$).

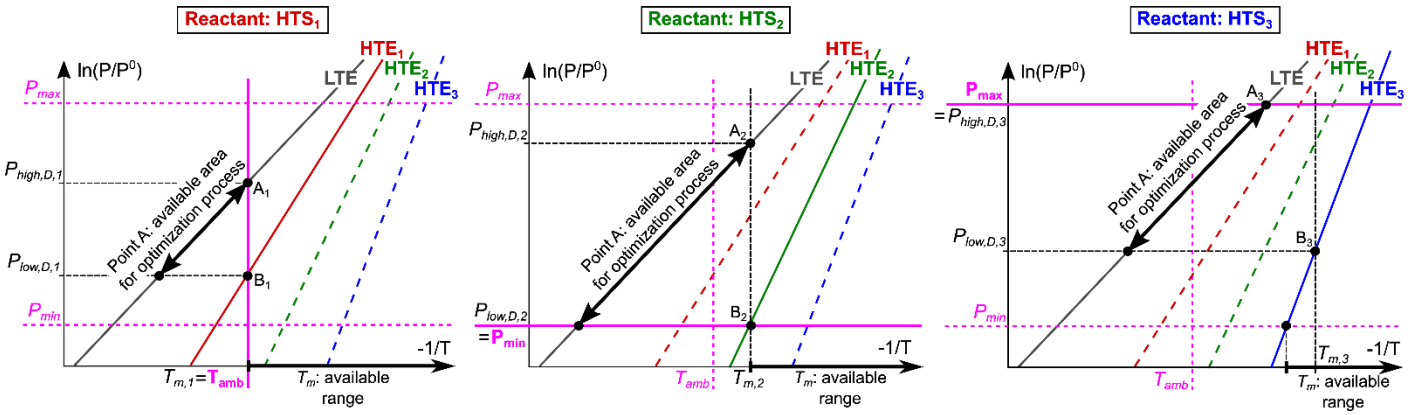

Fig. 6 – Process used to define the main temperature and pressure levels of the autothermal step,

highlighted for three reactive salts (temperature pinches are neglected).
Points A refer to points 13-1 and points B refer to points 5-6 in Figs. 2-5.
First step: Temperature T_m is set in the range complying with the constraints (ii) and (iv) (thick line on x-axis).
Second step: an optimization process allows to set point A in compliance with constraints (i), (iii) and (v).

To find the most favorable operating temperature T_m in terms of energy performance of the cycle, the effects of T_m on pressure ratio $R_p=P_3/P_{3'}$ and specific work output w are analyzed.

For this study, only one cycle configuration and a few representative reactive salts are selected (similar trends can be observed for other configurations and reactive salts). The operating mode used for the calculations is the discharge power generation mode. The single sorption cycle is chosen as it is the most innovative configuration (resorption cycles are much more studied in the literature). Moreover, two well-known reactive salts are used, whose heat source temperatures are spread along the considered temperature range ($T_{hot} < T_{hot,max} = 250°C$): $CaCl_2$ (8/4)NH_3 (requiring $T_{hot} = 108°C$ as heat source temperature) and $MnCl_2$ (6/2)NH_3 ($T_{hot} = 171°C$). For several values of T_m, the maximization process described above was carried out. The results of this study are given in *Fig. 7*. Several key observations can be underlined:

- For the reactant $CaCl_2$ (8/4)NH_3 (red symbols), the minimal value of T_m is determined by the operating constraint (ii) $T_m > T_{amb} = 20°C$: this reactive salt is representative of HTS_1 in *Fig. 6*.
- For the reactant $MnCl_2$ (6/2)NH_3 (green symbols), the minimal value of T_m is determined by the constraint on low pressure (iv) $P_{low,D} > P_{min}$: in this case, the minimal values of T_m is $T_{eq,HTE}(P_{min}) = 40.2°C$. This reactive salt is representative of HTS_2 in *Fig. 6*.
- The case HTS_3 is not depicted in *Fig. 7* because quite a few reactants highlight the operating constraint (v) $P_{high,D} \leq P_{max}$. Indeed, this constraint is not very limiting in discharging step. However, one example is $SnBr_2$ (2/1)NH_3: this reactive salt is representative of HTS_3 in *Fig. 6*, because $P_{high,D}$ is bounded by P_{max} in the autothermal discharging step (see *Fig. 8*b).
- Pressure ratio R_p decreases when T_m increases. This is due to the higher slope of the HTE line compared to the LTE line in the Clausius-Clapeyron diagram.
- Because of the decrease in R_p, specific work output w also decreases when T_m increases.

In conclusion to this analysis, the temperature T_m of the autothermal discharging step must be set at the minimal achievable value (according to the constraints (ii) $T_m \geq T_{amb}$ and (iv) $P_{low,D} \geq P_{min}$) to optimize the energy performance of the cycle. This process was applied to obtain the results presented in Sections 4 and 5.

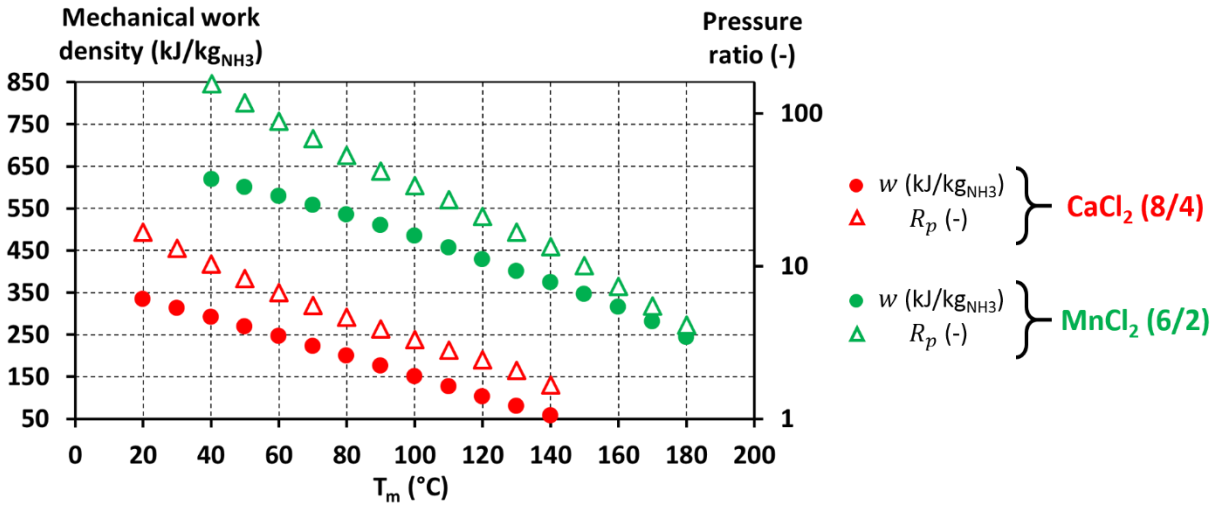

Fig. 7 – Influence of the temperature level T_m of the autothermal discharging step on power production: mechanical work density w (left scale, circles) and pressure ratio R_p (right scale, triangles).
Red symbols: $CaCl_2$ (8/4)NH_3 (corresponding to HTS_1 in Fig. 6: constraint (ii) sets the minimum value of T_m).
Green symbols: $MnCl_2$ (6/2)NH_3 (corresponding to HTS_2 in Fig. 6: constraint (iv) sets the minimum value of T_m).

4. Discharge power generation mode

As detailed in Section 2.1, the **discharge** power generation mode of hybrid thermochemical cycles comprises an isobaric charging step (non-productive step, points 7 to 12) and a non-isobaric discharging step (points 13 to 6) enabling power production through the coupling of thermal and mass flows between vapor-generating component (LT reactor or evaporator) and vapor-consuming component (HT reactor). We note that

according to the HTS, the low pressure $P_{low,D}$ may be constrained by the technological boundary value P_{min} (see Section 3.4).

4.1. Operating conditions

The operating conditions of the cycles are shown in *Fig. 8* (temperature levels T_m and T_{hot} and pressure levels) and *Fig. 9* (volumetric expansion ratios). On the *x*-axis, the selected salts (HTSs) are ranked according to their equilibrium temperature at $P = P^0 = 1$ bar (increasing values).

The behaviors of the operating temperature (T_m) and operating pressures ($P_{low,D}$ and $P_{high,D}$) of the autothermal discharging step are driven by the three external constraints highlighted in Section 3.4 ((ii) $T_m \geq T_{amb}$, (iv) $P_{low,D} \geq P_{min}$ and (v) $P_{high,D} \leq P_{max}$), knowing that T_m is always set at the minimal operable value (as explained in Section 3.4). These three constraints arise in *Fig. 8*b (single sorption cycle):

- A first set of reactants (from $CaCl_2$ (8/4)NH_3 to $CaBr_2$ (6/2)NH_3) is representative of HTS_1 in Section 3.4 (red line HTE_1 in *Fig. 6*): T_m remains constant at $T_{amb} = 20$°C (constraint (ii): $T_m = T_{amb}$, thus $P_{low,D} = P_{eq,HTE}(T_{amb})$), while the low pressure $P_{low,D}$ gradually decreases.
- The following reactants (from $ZnCl_2$ (4/2)NH_3 to SnI_2 (2/1)NH_3) are representative of HTS_2 in Section 3.4 (green line HTE_2 in *Fig. 6*): the low pressure $P_{low,D}$ reaches the limit value P_{min} (constraint (iv): $P_{low,D} = P_{min}$, thus $T_m = T_{eq,HTE}(P_{min})$), while T_m and $P_{high,D}$ gradually increase.
- The last reactants (from $ZnBr_2$ (4/2)NH_3 to $CuSO_4$ (4/2)NH_3) are representative of HTS_3 in Section 3.4 (blue line HTE_3 in *Fig. 6*): $P_{high,D}$ reaches the limit value P_{max} (constraint (v): $P_{high,D} = P_{max}$).

Similar trends are observed in *Fig. 8*a (resorption cycle), although T_m is always strictly higher than T_{amb} and $P_{high,D}$ is always strictly lower than P_{max}. We note that T_m reaches 101°C for resorption cycles and 85°C for single sorption cycles.

The heat source temperature T_{hot} shows an increasing trend, since the reactive salts are ranked by increasing equilibrium temperature at $P = P^0 = 1$ bar. For the selected reactants (according to the selection process described in Section 3.3), the minimal required heat source temperature is 164°C for resorption cycle (see *Fig. 8*a), and only 108°C for single sorption cycle (see *Fig. 8*b). This is because single sorption cycle takes advantage of ammonia liquid/vapor phase change as LTE (lower equilibrium temperatures than the LTS used in resorption cycle, $BaCl_2$ (8/0)NH_3).

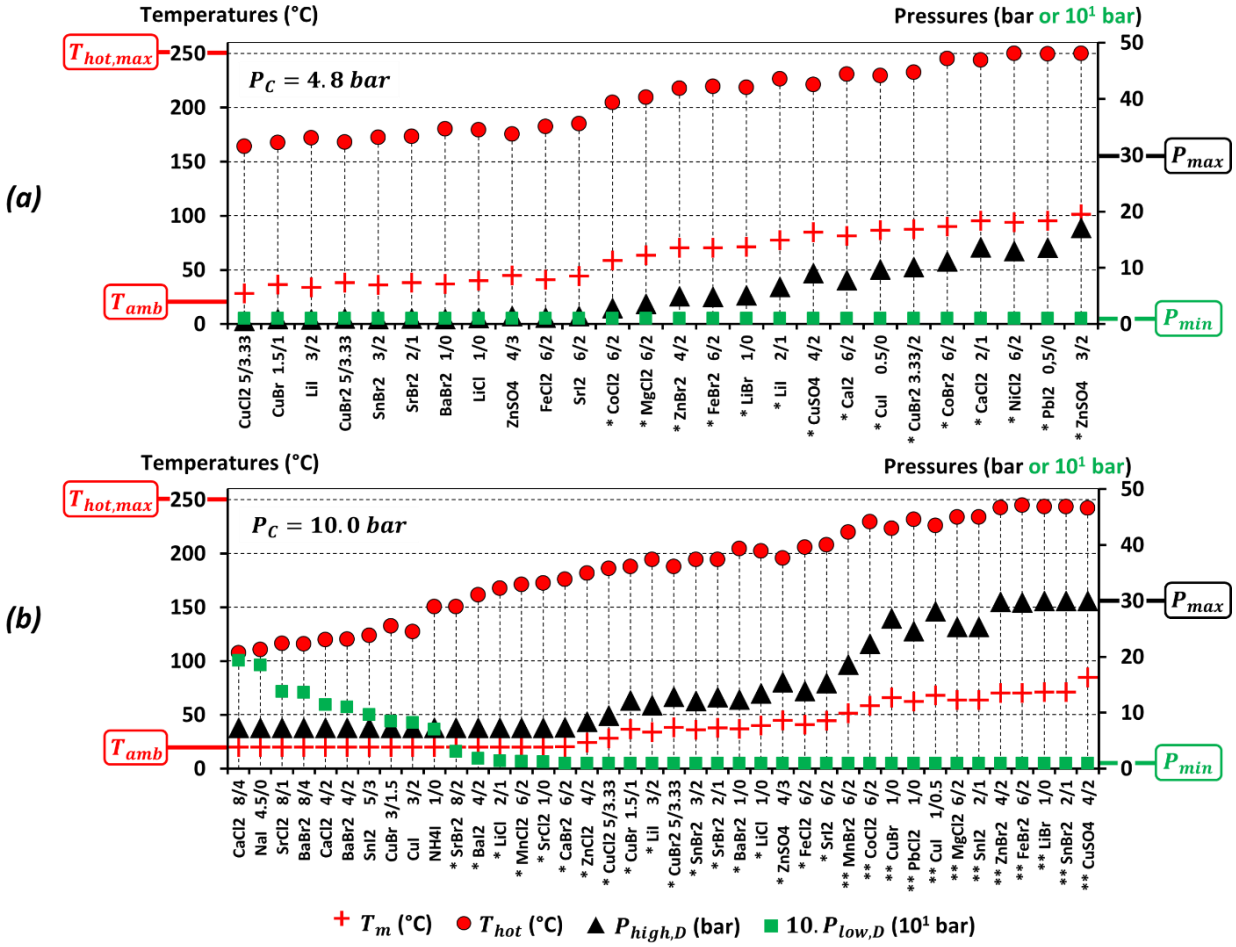

Fig. 8 – Discharge power generation mode: operating conditions of the hybrid cycle for selected salts (temperatures and pressures).

***(a)** Resorption cycle **(b)** Single sorption cycle*

**: 2-expansion configuration **: 3-expansion configuration*

Finally, several technical configurations (using one, two or three expansion stages, to comply with the technological constraint $R_v < R_{v,max} = 10$) were investigated and are highlighted in *Figs. 8-9* with asterisks before the name of the HTS. Volumetric expansion ratios $R_{v1,D}$, $R_{v2,D}$ and $R_{v3,D}$ (*Fig. 9*) show an overall increasing trend, and discontinuities arise when an expansion stage is added.

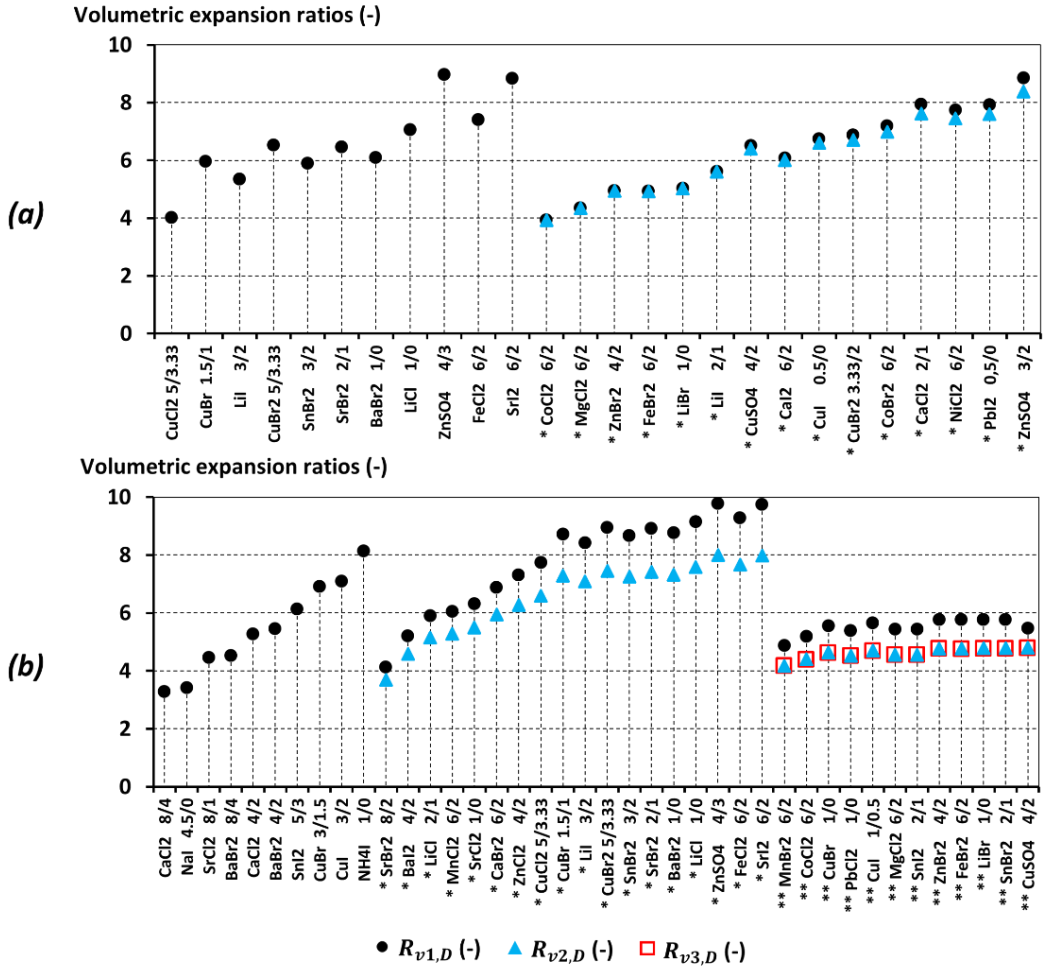

Fig. 9 – Discharge power generation mode: operating conditions of the hybrid cycle for selected salts (volumetric expansion ratios).
***(a)** Resorption cycle **(b)** Single sorption cycle*
**: 2-expansion configuration **: 3-expansion configuration*

4.2. Energy and exergy performances

In *Fig. 10*, the energy and exergy efficiencies of resorption (a) and single sorption (b) cycles are plotted as a function of the reactive salts (ranked as in *Figs. 8-9*). For these two performance criteria, an increasing trend is observed because the increasing expansion ratio ($R_{v,D}$, see *Fig. 9*) results in an increasing power output.

We note that η_{ex} has higher values than η_I. This is due to the high exergy content of the useful effects of the cycle (the main output is power, as indicated by the high values of power production ratios τ_w, see *Fig. 11*). The good values of η_{ex} compared with η_I are discussed later, in the light of Eq. **(24)** and *Fig. 11*.

Efficiencies are lower for the resorption cycle than for the single sorption cycle:

- η_I ranges from 0.06 to 0.15 in *Fig. 10*a and from 0.08 to 0.21 in *Fig. 10*b. This energy performance difference is due to the fact that the available pressure ratio ($P_3/P_{3'}$ in *Fig. 2*) is lower in the resorption cycle than in the single sorption cycle (because of the closeness of LTE and HTE lines in the resorption case), which leads to a lower power output.
- η_{ex} ranges from 0.11 to 0.28 in *Fig. 10*a and from 0.20 to 0.33 in *Fig. 10*b**.** This exergy performance difference is due (i) to the above-mentioned power output difference between resorption and single sorption cycles, and (ii) to the higher heat source temperatures in the resorption cycle compared to the single sorption cycle (see *Fig. 8*).

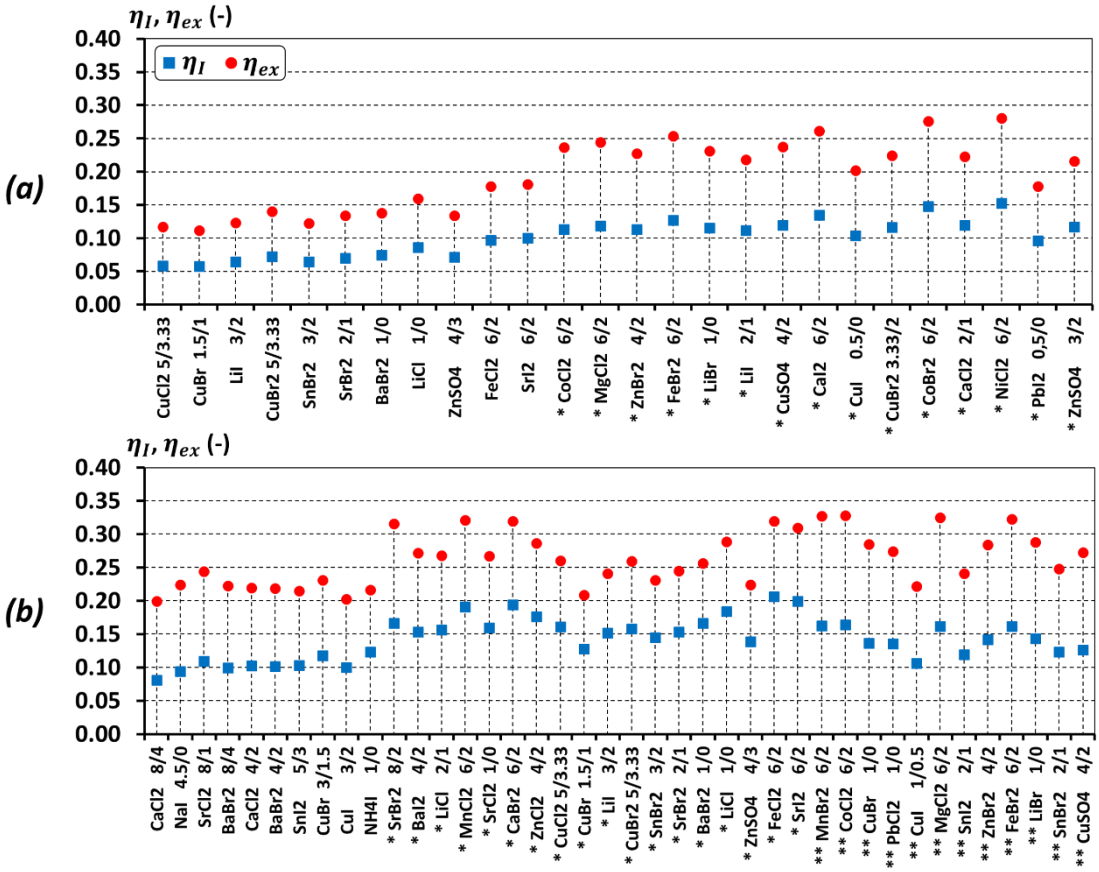

Fig. 10 – Discharge power generation mode: energy and exergy efficiencies of the cycle for selected salts.
***(a)** Resorption cycle* ***(b)** Single sorption cycle*

The last two performance criteria (w and $w+ex_{cold}$) are given in *Fig. 11*, along with power production ratio τ_w. Firstly, we note that Equations from **(17)** to **(23)** can yield the following expression:

$$\frac{\eta_{ex}}{\eta_I} = \frac{\tau_w + (1-\tau_w).(T^0/T_{cold} - 1)}{(1 - T^0/T_{hot})} \qquad \textbf{(24)}$$

Eq. **(24)** shows that τ_w and T_{hot} are the variables influencing the ratio η_{ex}/η_I. Considering their respective variation ranges, it appears that the ratio η_{ex}/η_I is mainly driven by τ_w. This relationship explains the discontinuities highlighted in *Figs. 10-11*:

- In *Figs. 10*a and *11*a, a discontinuity arises between SrI_2 (6/2)NH_3 and $CoCl_2$ (6/2)NH_3: τ_w increases from 62.5 % to 79.1 % (*Fig. 11*a), increasing the difference between η_I and η_{ex} (*Fig. 10*a: η_{ex}/η_I changes from 1.8 to 2.1).
- Similarly, *Figs. 10*b and *11*b highlight a discontinuity between SrI_2 (6/2)NH_3 and $MnBr_2$ (6/2)NH_3: τ_w increases from 57.4 % to 80.0 % (*Fig. 11*b), increasing significantly the difference between η_I and η_{ex} (*Fig. 10*b: η_{ex}/η_I rises from 1.5 to 2.0).

Two areas are highlighted in *Fig. 11*:

- τ_w remains almost constant for a large proportion of the reactants (left area): cold production is provided at the outlet of the expander, taking advantage of the low value of $T_{3'}$ (see *Fig. 2*). Power production ratio ranges from 62.5% to 62.9% in the resorption cycle (*Fig. 11a*), and from 50.3% to 57.5% in the single sorption cycle (*Fig. 11b*).
- For the last reactive salts (right area, highest equilibrium temperatures), two or three expansion stages are needed to take full advantage of the high available pressure ratio. Temperatures at the outlet of each expander are slightly higher than in the one-expansion case, so a lower cold production is obtained. Consequently, τ_w reaches higher values than for the previous reactants, ranging from 79.1% to 79.6% in the resorption cycle, and from 80.0% to 92.3% in the single sorption cycle.

The difference is quite small for specific work output (green areas) and exergy output (blue areas): mechanical work forms a very large proportion of exergy output, because it has a higher exergy content than cold production, and power production ratio τ_w exhibits high values (always higher than 50%). $w+ex_{cold}$ increases from 168 kJ/kg$_{NH3}$ to 555 kJ/kg$_{NH3}$ for the resorption cycle, and from 133 kJ/kg$_{NH3}$ to 609 kJ/kg$_{NH3}$ for the single sorption cycle.

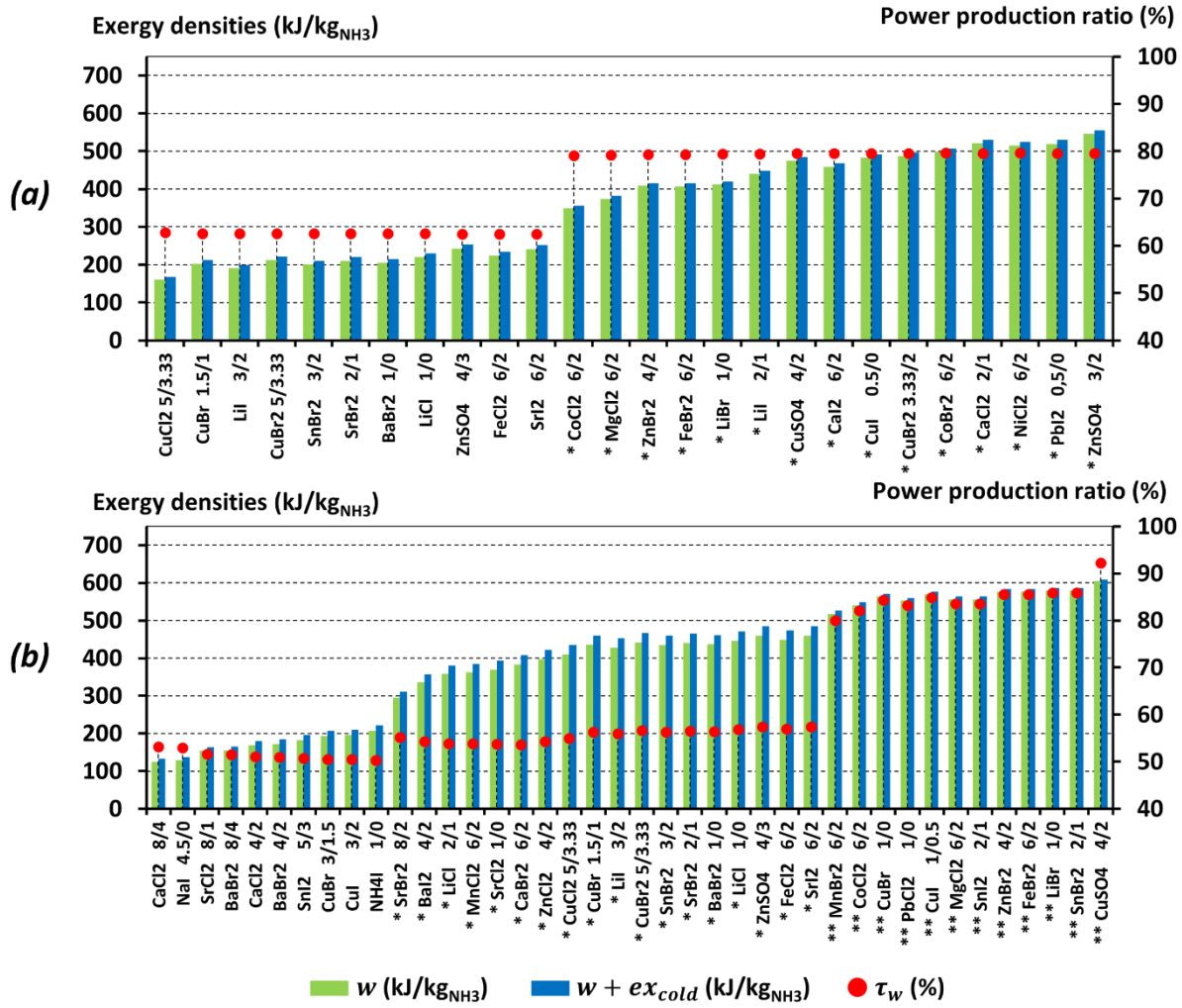

Fig. 11 – Discharge power generation mode: exergy densities and power production ratio.
***(a)** Resorption cycle* ***(b)** Single sorption cycle*

5. Combined charge and discharge power generation mode

As detailed in Section 2.3, in the **combined charge and discharge** power generation mode, power is generated in both operating steps of the cycle: charging step (points 7 to 12, see *Figs. 3* and *5*) and discharging step (points 13 to 6). This mode faces two constraints on its operating pressures: in the discharging step, as for the previous case, $P_{low,D}$ may be constrained by the technological limit value on low pressure ($P_{low,D} > P_{min}$); in the charging step, the constraint on the high pressure value can become a limiting factor ($P_{high,C} < P_{max}$).

5.1. Operating conditions

Operating conditions are first plotted in *Fig. 12* (T_m, T_{hot} and pressure levels) and *Fig. 13* (volumetric expansion ratios $R_{v,C}$ and $R_{v,D}$). The operating conditions of the autothermal discharging step (temperature T_m, pressures $P_{low,D}$ and $P_{high,D}$) show similar trends to that in the discharge power generation mode (*Fig. 8*). Focusing on the resorption cycle (*Fig. 12*b):

- A first set of reactants (from $BaCl_2$ (8/0)NH_3 to $CaBr_2$ (6/2)NH_3) is representative of HTS_1 in Section 3.4 (red line HTE_1 in *Fig. 6*): T_m remains constant at $T_{amb} = 20°C$ (constraint (ii) applies: $T_m = T_{amb}$, and thus $P_{low,D} = P_{eq,HTE}(T_{amb})$), while the low pressure $P_{low,D}$ gradually decreases.

- The following reactants (from $ZnCl_2$ (4/2)NH_3 to $MgCl_2$ (6/2)NH_3) are representative of HTS_2 in Section 3.4 (green line HTE_2 in *Fig. 6*): the low pressure $P_{low,D}$ reaches the limit value P_{min} (constraint (iv) applies: $P_{low,D} = P_{min}$, thus $T_m = T_{eq,HTE}(P_{min})$), while T_m and $P_{high,D}$ gradually increase.
- For all the selected reactants, high pressure $P_{high,D}$ remains strictly lower than P_{max}, so that the case of HTS_3 in Section 3.4 (when constraint (v) applies: $P_{high,D} = P_{max}$) is not illustrated in *Fig. 12*.

Finally, we note that T_m reaches lower values than in discharge power generation mode: 94 °C in the resorption cycle and 68 °C in the single sorption cycle.

The heat source temperature T_{hot} also shows a similar increasing trend to that in discharge power generation mode (*Fig. 8*), but shifted towards higher values, because the charging step is non-isobaric. The minimal value of T_{hot} is 185 °C in the resorption cycle (using $SrBr_2$ (8/2)NH_3 as HTS, see *Fig. 12a*), and 117 °C in the single sorption cycle (using $BaCl_2$ (8/0)NH_3 as HTS, see *Fig. 12b*).

Regarding the volumetric expansion ratio of charging step ($R_{v,C}$, see *Fig. 13*), two areas are highlighted:

- $R_{v,C}$ remains constant for a large proportion of the HTSs, because the high pressure $P_9 = P_{high,C}$ of the charging step is constrained by its maximal value P_{max}, and pressure $P_{9'} = P_{low,C}$ is fixed by the ambient heat sink (T_{amb}) and the position of the LTE line. For these reactants, $R_{v,C}$ is set at 4.7 in the resorption cycle and 2.5 in the single sorption cycle.
- For the last reactants, $R_{v,C}$ slightly decreases because heat source temperature T_{hot} has reached the upper limit $T_{hot,max} = 250$ °C: to keep $T_{hot} = T_{hot,max}$, the high pressure $P_9 = P_{high,C}$ is reduced, causing the decrease in $R_{v,C}$.

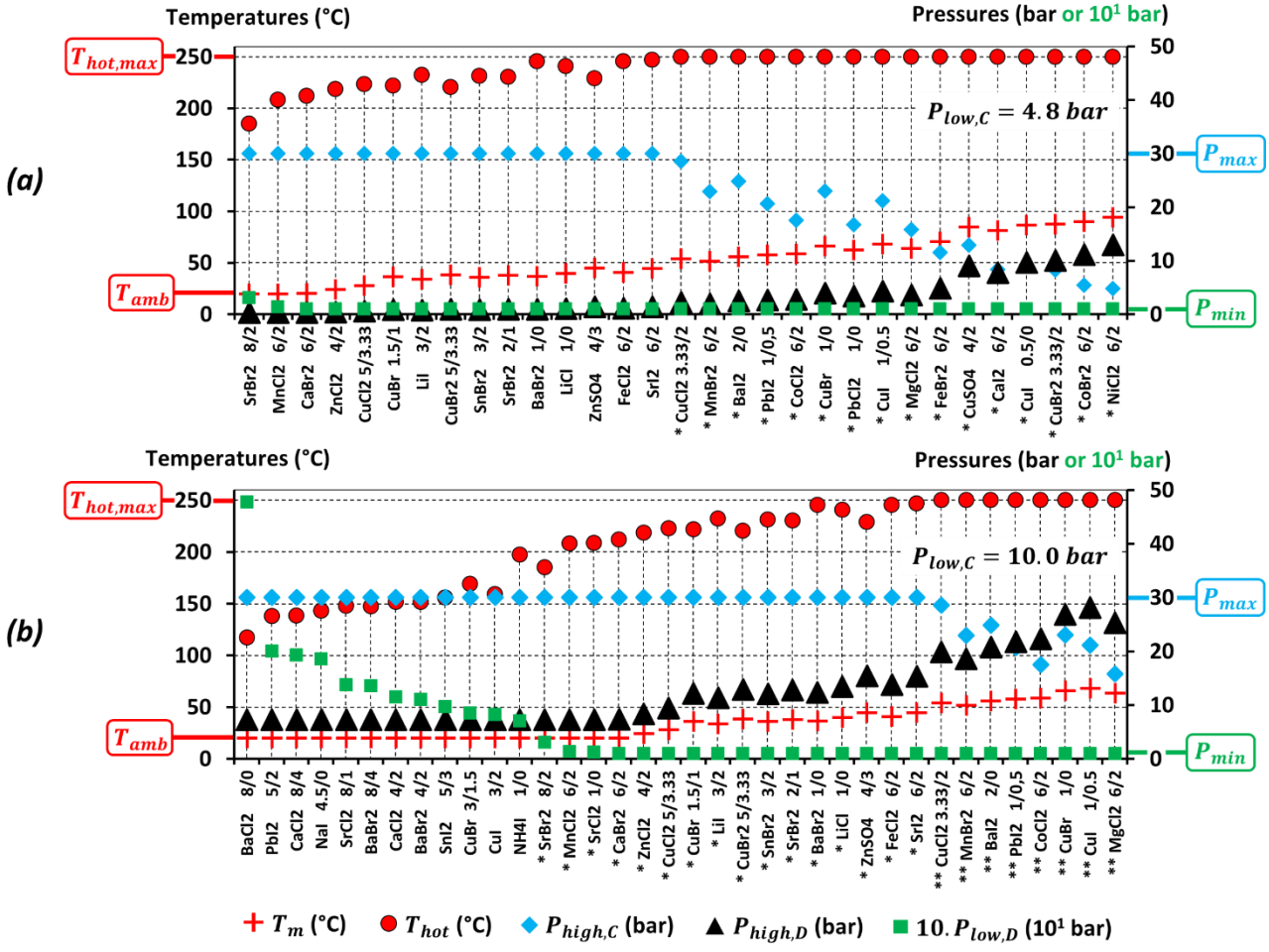

Fig. 12 – Combined charge and discharge power generation mode:
operating conditions of the hybrid cycle for selected salts (temperatures and pressures)
***(a)** Resorption cycle **(b)** Single sorption cycle*
**: 2-expansion configuration **: 3-expansion configuration*

Finally, the volumetric expansion ratios of the discharging step ($R_{v1,D}$, $R_{v2,D}$, $R_{v3,D}$ plotted in *Fig. 13*) behave similarly to the discharge power generation mode (*Fig. 9*): they show increasing trends, with small discontinuities when expansion stages are added.

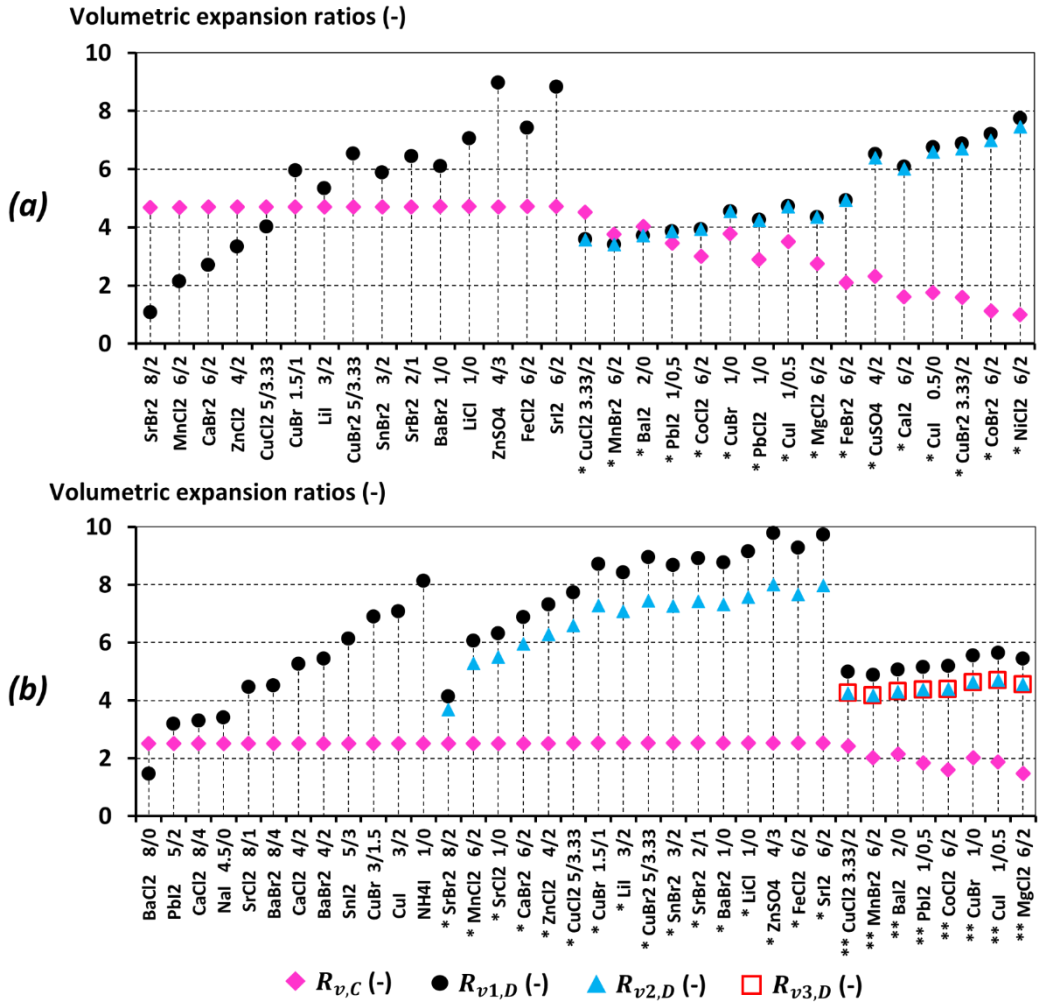

Fig. 13 – Combined charge and discharge power generation mode:
operating conditions of the hybrid cycle for selected salts (volumetric expansion ratios)
***(a)** Resorption cycle* ***(b)** Single sorption cycle*
: 2-expansion configuration* *: 3-expansion configuration*

5.2. Energy and exergy performances

Fig. 14 displays the energy and exergy efficiencies for combined charge and discharge power generation mode. Similar to the discharge power generation mode (see *Fig. 10*), the values of these performance criteria increase when the HTS equilibrium temperature increases. However, this increasing trend is mitigated by the decrease in the amount of mechanical work produced in the charging step for the last reactive salts, due to the above-mentioned decrease in $R_{v,C}$.

For similar reasons as discussed in Section 4 for discharge power generation mode, both energy and exergy efficiencies are lower for resorption cycle than for single sorption cycle:

- η_I ranges from 0.08 to 0.16 in resorption cycle (*Fig. 14*a) and from 0.07 to 0.24 in single sorption cycle (*Fig. 14*b).
- η_{ex} ranges from 0.18 to 0.32 in resorption cycle (*Fig. 14*a) and from 0.20 to 0.40 in single sorption cycle (*Fig. 14*b).

Finally, *Fig. 15* gives a quantified overview of the useful effects of the cycles, through the performance criteria w and $w+ex_{cold}$ and the variable τ_w. Concerning the power production ratio, the analysis of Section 4 is suitable to describe its behavior, since two areas can be observed in the same way as in *Fig. 11*. The difference from discharge power generation mode lies in its values: τ_w ranges from 78.3% to 100% in resorption cycles, and

from 62.7% to 100% in single sorption cycles. These values are higher than those obtained in Section 4, owing to the additional power production in the charging step.

The specific work and exergy outputs w and $w+ex_{cold}$ are also much higher than in discharge power generation mode. Thus $w+ex_{cold}$, increases from 261 kJ/kg$_{NH3}$ to 663 kJ/kg$_{NH3}$ in resorption cycle and from 170 kJ/kg$_{NH3}$ to 722 kJ/kg$_{NH3}$ in single sorption cycle. We note that the fluctuating values observed for the last reactive salts are caused by the decrease in power production in the charging step (in connection with the decrease in $R_{v,C}$, see *Fig. 11*).

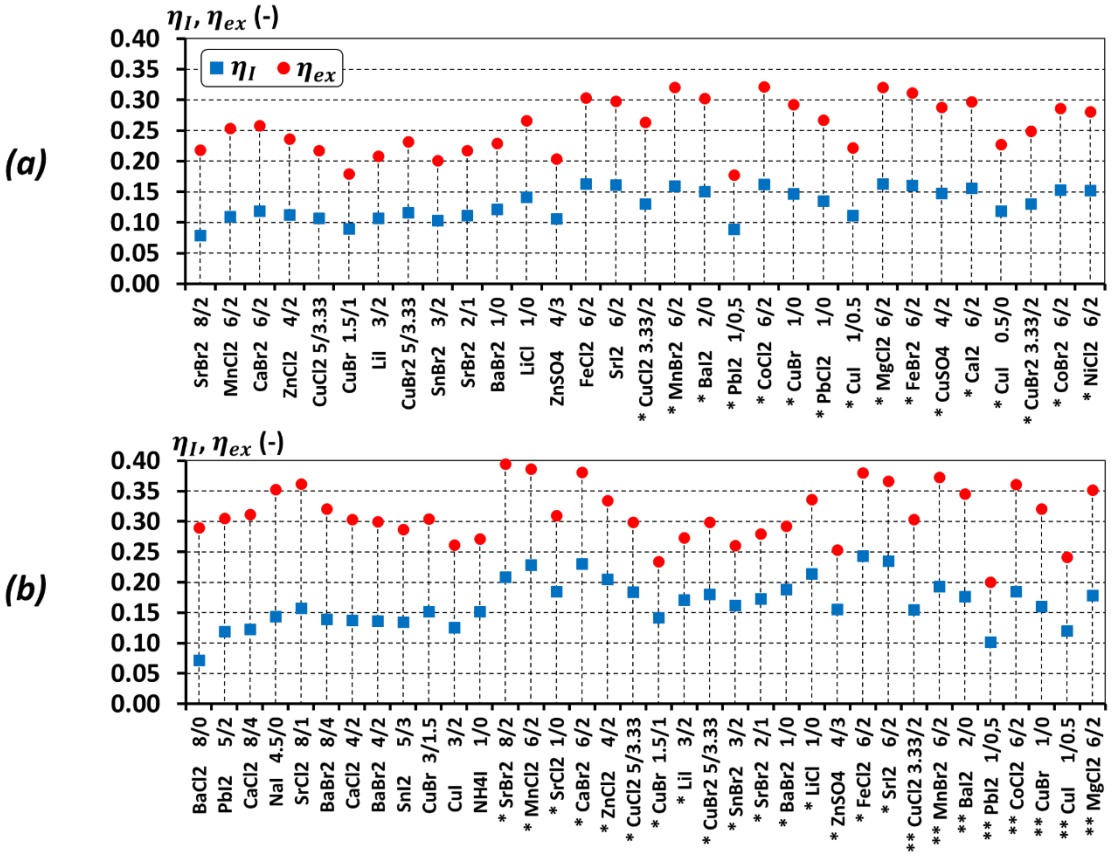

Fig. 14 – Combined charge and discharge power generation mode: energy and exergy efficiencies of the cycle for selected salts.
***(a)** Resorption cycle* ***(b)** Single sorption cycle*

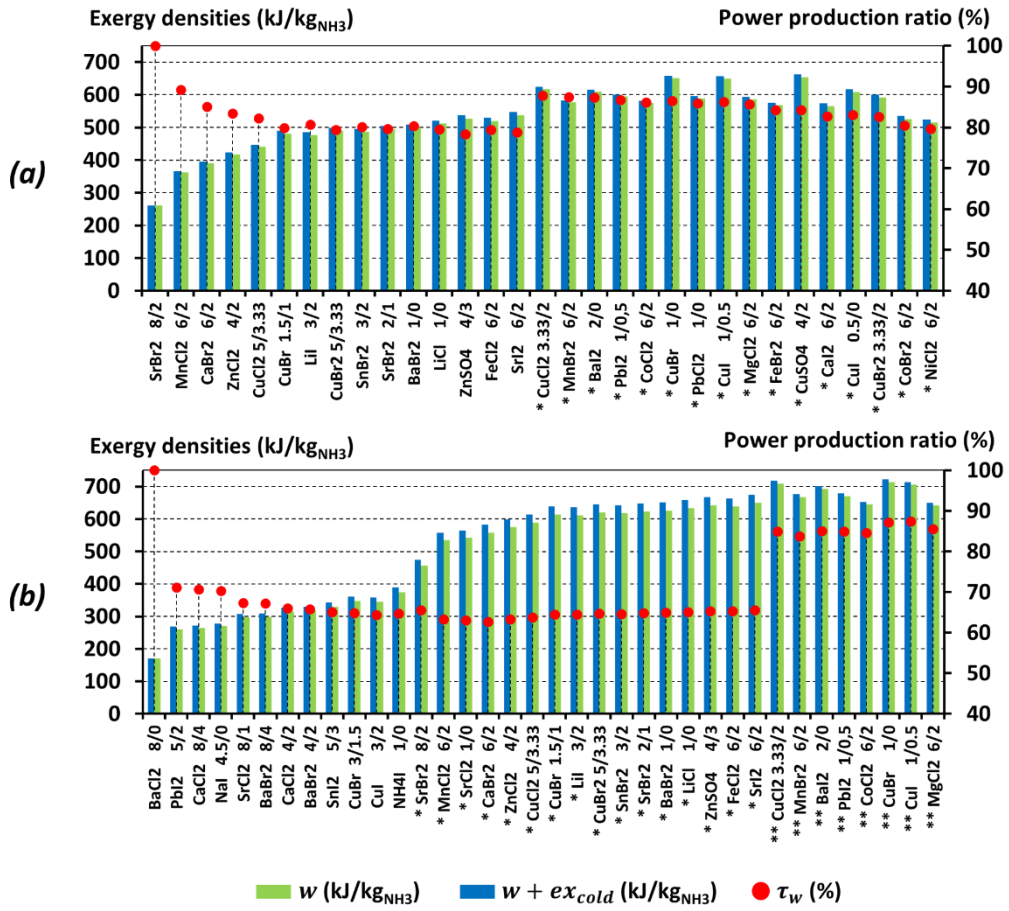

Fig. 15 – Combined charge and discharge power generation mode: exergy densities and power production ratio.
***(a)** Resorption cycle* ***(b)** Single sorption cycle*

6. Discussion of the results

The following section contains a discussion of the results presented in Sections 4 and 5. The first part of this discussion is based on a sensitivity study (Section 6.1): in this sensitivity study, the effects of changing some key parameter values of the model on energy and exergy performances of the cycles are studied. The effects of uncertainty on thermochemical data of the reactive salts (enthalpy and entropy of reaction) are also discussed. A concise summary of the main performance and operating conditions is then proposed (Section 6.2) to identify the most relevant applications of these hybrid cycles.

6.1. Sensitivity of the results to some key parameters

Although the parameter values provided in Section 3.1 are considered realistic, some deviations from these values could be observed in practical implementations (for example: temperature pinches ΔT_{HX1}, ΔT_{HX2}, ΔT_{eq} and characteristics of the components such as isentropic efficiency η_{is}, ratio of metal to composite volume τ_{met}, range of reaction advancement ΔX). In addition, according to the technical facilities, the limit pressures P_{min} and P_{max} can be set at different values from those stated in Section 3.2. T_{amb} is also a fluctuating parameter in real-world process operation. A sensitivity analysis is therefore needed to assess the effects of these key parameters on the performance of the cycles.

Since the thermodynamic model involves a large number of parameters (e.g. thermodynamic and heat transfer parameters, characteristics of the components, thermochemical data), four performance criteria (see Section 3.3, Eqs. **(17)**-**(20)**) and four cycle designs (two operating modes and two layouts: see Sections 2.2, 2.3 and 2.4), the following choices have been made to restrict the amount of data in the results of the sensitivity study:

(i) Relevant key parameters and related variation ranges: the selected parameters are listed in *Table 1*, with their realistic ranges of variation. They are considered the most relevant for this sensitivity study because they are potential control parameters.

(ii) Relevant performance criteria: energy efficiency η_I and specific exergy output $w+ex_{cold}$ are selected because they provide a good overview of energy and exergy performances and they contain both qualitative (through the dimensionless energy ratio η_I) and quantitative (through the specific extensive quantity $w+ex_{cold}$) information.

(iii) Cycle design (operating mode and configuration: resorption or single sorption): the combined charge and discharge power generation mode emerges as the most relevant operating mode because it is sensitive to variations of both low and high pressure limit values. Moreover, the single sorption cycle is selected for this study because it is the most innovative configuration.

(iv) Set of reactive HTSs: the three reactants $CaCl_2$ (8/4)NH_3, $SrCl_2$ (8/1)NH_3 and $SrBr_2$ (8/2)NH_3 are selected as representative HTSs because they are well-known salts, dispatched over various heat source temperatures (T_{hot} values are 138, 148 and 185 °C, respectively).

The sensitivity analysis is carried out with EES software [28]: for a given reactive HTS, a set of 10 simulations (calculation of the thermodynamic path and performances of the cycle) is performed for each studied parameter (using 10 values uniformly distributed in its variation range). Finally, the minimum and maximum values of the performance criteria η_I and $w+ex_{cold}$ are retrieved.

Parameter	P_{min} (bar)	P_{max} (bar)	τ_{met} (-)	η_{is} (-)	ΔT_{r-eq} (K)	T_{amb} (°C)
Variation range [min; max]	*[0.1; 1]*	*[30; 100]*	*[0; 0.3]*	*[0.7; 0.9]*	*[10; 40]*	*[15; 25]*

Table 1 – Chosen parameters and their variation ranges for the sensitivity study.

The results are presented in *Fig. 16*. For each salt and each of the six chosen parameters (see *Table 1*), the sensitivity of the two above-mentioned performance criteria is displayed: energy efficiency η_I (red lines) and specific exergy output $w+ex_{cold}$ (green dotted lines). These sensitivities are plotted as relative deviations with respect to the nominal value of the variable: $\Delta(\eta_I)/\eta_{I,nom}$ and $\Delta(w+ex_{cold})/(w+ex_{cold})_{nom}$. The symbols (respectively red filled and green empty symbols) represent the extremal deviations obtained in the variation range of the parameter studied.

The main conclusions are listed below:

- The most influential parameter is $\Delta T_{r\text{-}eq}$ (triangles): the relative deviations $\Delta(\eta_I)/\eta_{I,nom}$ and $\Delta(w+ex_{cold})/(w+ex_{cold})_{nom}$ range respectively from −50.1% to 26.0% and from −26.7 to 15.0%. A small change in the temperature pinch $\Delta T_{r\text{-}eq}$ causes relatively strong modifications of the thermodynamic cycle in *Fig. 3*, in both charging and discharging steps (since $\Delta T_{r\text{-}eq}$ drives the gap between points 4-5 and 8-9).
- The performance is also highly sensitive to parameter P_{max}, especially $w+ex_{cold}$ (green dotted lines) whose maximal relative deviation ranges from 29.3% to 38.3%. An increase in the limit pressure P_{max} enables a higher expansion stage in the charging step (higher pressure ratio $P_9/P_{9'}$ in *Fig. 3*), and so power production is strongly enhanced.
- The variation of the technological boundary value P_{min} (rectangles) in the chosen range does not modify the cycle in the cases of $CaCl_2$ (8/4)NH_3 or $SrCl_2$ (8/1)NH_3 as HTS. However, for $SrBr_2$ (8/2)NH_3 as HTS, a decrease in the cycle performance is observed when P_{min} increases: relative deviations reach −11.7% for η_I and −8.9% for $w+ex_{cold}$. Since the HTE line of $SrBr_2$ (8/2)NH_3 is shifted towards higher temperatures than $CaCl_2$ (8/4)NH_3 and $SrCl_2$ (8/1)NH_3, pressure $P_{3'} = P_{low,D}$ is lower (for a fixed value of $\Delta T_{r\text{-}eq}$, see *Fig. 3*) and therefore more sensitive to a change in P_{min}.
- For the other parameters studied, relative deviations are weaker: both $\Delta(\eta_I)/\eta_{I,nom}$ and $\Delta(w+ex_{cold})/(w+ex_{cold})_{nom}$ lie in the range [−13.5; 13.5%].

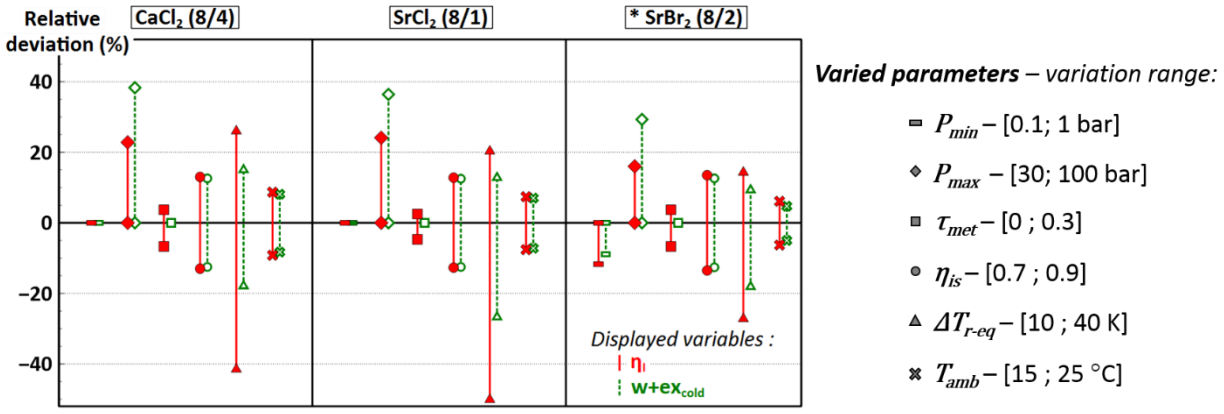

Fig. 16 – Sensitivity analysis for combined charge and discharge power generation mode (single sorption cycle). Symbols are the extremal relative deviations of η_I (red) and $w+ex_{cold}$ (green) with respect to their nominal values: minimal and maximal values of $\Delta(\eta_I)/\eta_{I,nom}$ (red symbols) and $\Delta(w+ex_{cold})/(w+ex_{cold})_{nom}$ (green symbols)

Beside the sensitivity of performance results to the key parameters of the thermodynamic model, the main error sources should be discussed:

- Regarding numerical errors, the equation-solving program EES uses a variant of Newton's method [28] to provide a numerical solution to the set of coupled algebraic equations (energy balance equations and equations describing thermodynamic transformations throughout the cycle). A solution is considered to be found if the maximum relative residual value for all equations is less than the Residual Tolerance $\varepsilon = 1.10^{-6}$, which is negligible compared to the other possible sources of errors.
- Regarding other sources of errors, among input parameters, the thermodynamic data of the reactive salts are the most likely to contain errors. On this issue, most of the data used for this study are known with a good accuracy (especially for metallic chlorides, and to a lower extent for bromides and iodides). Based on the experimental uncertainties provided by Wentworth et al. [29], Böhringer [30] and Touzain [27], uncertainty propagation calculations have been conducted with EES software for the three reactants considered in this section. The results are displayed in *Table 2*. The relative uncertainties on performance criteria η_I and $w+ex_{cold}$ range from 5.0 % to 20.0 % and from 4.2 % to 21.8 %, respectively. Regarding $SrBr_2$ (8/2)NH_3, the high values are caused by the high uncertainties on thermochemical data (reaction enthalpy and entropy) for this reactive salt.

Uncertainties	$\Delta_r H^0$ (kJ.mol^{-1})	$\Delta_r S^0$ (J.mol^{-1}.K^{-1})	Ref.	η_I (-)	$w + ex_{cold}$ (kJ.kg$_{NH3}^{-1}$)
$CaCl_2$ (8/4)NH_3	41.0 ± **0.2**	134.4 ± **0.6**	[29]	0.12 ± **0.006** (*5.0 %*)	272.1 ± **11.31** (*4.2 %*)
$SrCl_2$ (8/1)NH_3	41.4 ± **0.4**	132.9 ± **1.3**	[30]	0.16 ± **0.012** (*7.5 %*)	308.2 ± **22.68** (*7.4 %*)
$SrBr_2$ (8/2)NH_3	45.6 ± **1.8**	133.6 ± **6.1**	[27]	0.21 ± **0.042** (*20.0 %*)	473.5 ± **103.2** (*21.8 %*)

Table 2 – Uncertainties on the thermodynamic data of the reactive salts (reaction enthalpy and entropy): effects on performance criteria η_I and $w+ex_{cold}$ (absolute and relative deviations)

Despite the uncertainties on thermochemical data of the reactants, the present paper enables identifying the main trends on energy and exergy performances of the cycles, which is the main purpose of this study.

6.2. Synthesis of the results

To compare the various modes and reactants set out in Sections 4 and 5, performance criteria η_I, η_{ex} and $w+ex_{cold}$ were picked out for each cycle and plotted (in *Figs. 17*, *18* and *19*) as functions of the heat source temperature T_{hot} required. In accordance with the methodology of this study (Section 3.3), for a given operating mode, each required hot source temperature matches one reactive salt.

As expected from a thermodynamic point of view, the three performance criteria show an overall increase with the raise of the heat source temperature T_{hot}. However, a deeper analysis shows that these trends are covering many information: the results are highly scattered (especially the efficiencies η_I and η_{ex}, see *Figs. 17* and *18*). The main reason for this scattering is the strong dependency of energy and exergy performances on the thermodynamic properties of the reactive salts: thermochemical data ($\Delta_r H^0$, $\Delta_r S^0$), stoichiometry and heat capacity of the reactants have a significant influence on heat input Q_{in}, and thus on energy and exergy efficiencies. Another reason is the setting of limit values in the thermodynamic study: $T_{hot,max}$ for heat source temperatures and technological limit values P_{min} and P_{max} for pressures (see *Figs. 8* and *12*). These limit values can bring significant changes in the thermodynamic path of the cycle (expansion stages, outlet temperature of the expanders), and thus in the power and cold productions. We note that a ceiling effect is observed at the limit temperature $T_{hot,max} = 250$ °C in *Figs. 17-19*: various energy and exergy performances are reached at this temperature level, according to the chosen HTS and cycle design (operating mode and configuration: resorption or single sorption).

These plots enable a comparison of performance between the two operating modes:

- The single sorption cycle in discharge mode (black triangles) is the only cycle that can be run with a heat source temperature under 100 °C (the lowest value for T_{hot} is 87 °C). However, for these temperatures, this cycle shows relatively weak performance. Better performance is reached at heat source temperatures of around 107 °C: η_I, η_{ex} and $w+ex_{cold}$ are respectively 0.08, 0.19 and 129 kJ/kg$_{NH3}$. Over the whole range of heat source temperatures, the maximum values are 0.21 for η_I, 0.33 for η_{ex} and 609 kJ/kg$_{NH3}$ for $w+ex_{cold}$.
- The resorption cycle in discharge mode (red triangles) requires higher heat source temperatures than the previous one (from 141 °C). Its performance is also lower: the maximum values are 0.15 for η_I, 0.28 for η_{ex} and 555 kJ/kg$_{NH3}$ for $w+ex_{cold}$. The resorption cycle thus seems less useful than the single sorption cycle.
- Similar trends are observed for the combined charge and discharge power generation mode. First, single sorption cycle (green squares) can operate over quite a wide range of heat source temperatures: the minimum value of T_{hot} is 117 °C. Owing to the additional power production in the charging step, higher energy and exergy performances are achieved: η_I, η_{ex} and $w+ex_{cold}$ reach respectively 0.24, 0.40 and 722 kJ/kg$_{NH3}$.
- Finally, the resorption cycle in combined charge and discharge mode (pink squares) requires a minimum heat source temperature of 185 °C, and is less efficient than the single sorption cycle within its range of T_{hot}: η_I, η_{ex} and $w+ex_{cold}$ reach respectively 0.16, 0.32 and 663 kJ/kg$_{NH3}$.

In the literature (see Section 1), energy and exergy efficiencies of hybrid thermochemical cycles range from 0.06 to 0.75 and from 0.41 to 0.90, respectively. These performances are obtained for heat source temperatures between 30 and 360 °C. For the novel hybrid cycles presented in this paper, *Figs. 17-19* show that energy and exergy efficiencies can reach 0.24 and 0.40, respectively. The range of required heat source temperatures is [87; 250 °C]. However, a fair comparison between literature and our results cannot be offered since very different assumptions are taken (especially for temperature pinches and heat source, heat sink and cold production temperatures).

To conclude this thermodynamic study, the main results are brought together in *Fig. 20*. This table gives an overview of the main features of each mode. The ability of the cycles to use low-grade heat sources and to provide useful effects with a high exergy content (power and additional refrigeration effect) is added using the variation ranges of variables T_{hot}, τ_w and $w+ex_{cold}$.

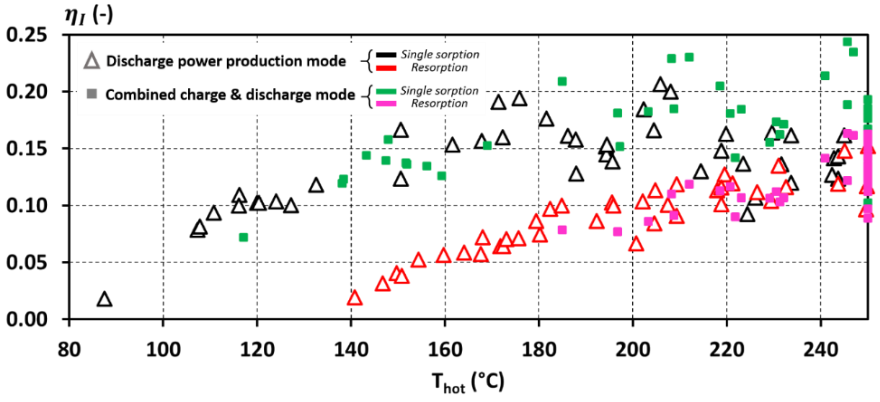

Fig. 17 – Energy efficiencies: summary of all selected salts for the four cycle designs (two operating modes and two layouts: resorption and single sorption)

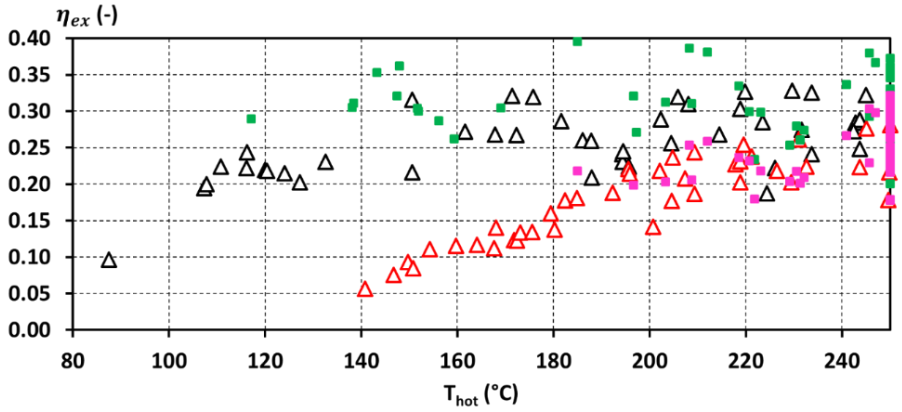

Fig. 18 – Exergy efficiencies: summary of all selected salts for the four cycle designs (two operating modes and two layouts: resorption and single sorption)

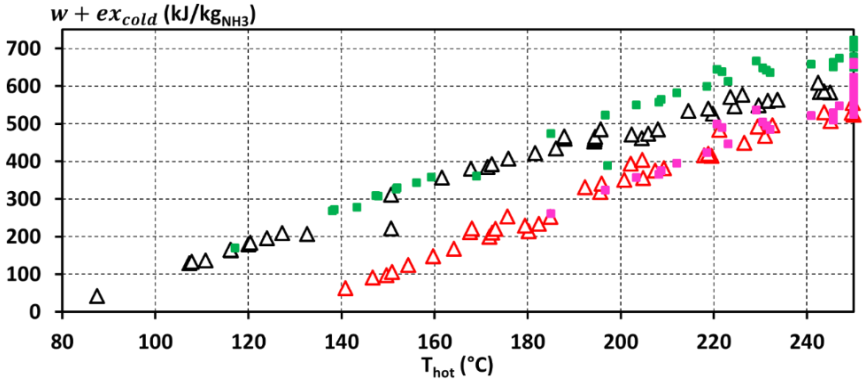

Fig. 19 – Specific exergy output: summary of all selected salts for the four cycle designs (two operating modes and two layouts: resorption and single sorption)

Characteristics:	**Discharge** mode		**Combined charge & discharge** mode	
	Resorption cycle	Single sorption cycle	Resorption cycle	Single sorption cycle
Valorization of low-grade heat	$T_{hot} > 141$ °C	$T_{hot} > 87$ °C	$T_{hot} > 185$ °C	$T_{hot} > 117$ °C
Proportion of power production	$\tau_w > 62.5$ %	$\tau_w > 50.3$ %	$\tau_w > 78.3$ %	$\tau_w > 62.7$ %
Storage of power production				
Specific exergy output (kJ/kg$_{NH3}$)	$64 < w + ex_{cold} < 535$	$42 < w + ex_{cold} < 584$	$262 < w + ex_{cold} < 663$	$170 < w + ex_{cold} < 722$

Performance level: ***Good*** ***Average*** ***Weak***

Fig. 20 – Overview of the advantages and weaknesses of each mode

7. Conclusions

In this paper, four novel hybrid thermochemical cycle designs (two operating modes and two configurations: *resorption* and *single sorption*) integrating an innovative autothermal working step were investigated and shown to be promising systems for low-grade heat storage and power and cold cogeneration with power output dominant. The main findings are listed below:

- An in-depth study highlighted that the optimum performance (highest power production) of the autothermal discharging step of the cycles is reached when the HTS synthesis temperature is as low as possible (i.e. ambient temperature or higher, according to the HTS).
- In **discharge** power generation mode, the single sorption cycle is the most attractive due to its lower heat source temperatures (from 107 °C) and higher performances (η_I reaches 0.21, η_{ex} reaches 0.33 and

$w+ex_{cold}$ reaches 609 kJ/kg$_{NH3}$) in comparison with the resorption cycle (minimum T_{hot} value is 141 °C and maximum performance values are 0.15 for η_I, 0.28 for η_{ex} and 555 kJ/kg$_{NH3}$ for $w+ex_{cold}$).

- In **combined charge and discharge** power generation mode, the additional power production in the charging step leads to better performances for both single sorption and resorption cycles. As in discharge power generation mode, the single sorption cycle operates over a wider range of heat source temperatures (from 117 °C) and achieves enhanced performances (η_I, η_{ex} and $w+ex_{cold}$ reach respectively 0.24, 0.40 and 722 kJ/kg$_{NH3}$) in comparison with the resorption cycle (minimum T_{hot} value is 185 °C and η_I, η_{ex} and $w+ex_{cold}$ reach respectively 0.16, 0.32 and 663 kJ/kg$_{NH3}$).
- The higher heat source temperatures and slightly weaker performances of resorption cycles when compared with single sorption cycles are due to the lower available pressure ratios, which lead to smaller power outputs. However, resorption cycles could be technically preferable to single sorption cycles since fewer expansion stages are involved at similar performance levels: a trade-off must be found between system complexity and performance.

The novel operating modes and the original comprehensive methodology used for their study add to the current body of knowledge in the field of hybrid thermochemical cycles. This extensive methodology allowed to identify the most promising reactants and the advantages and weaknesses of each operating mode in terms of low-grade heat valorization, power production and global exergy performances. Forthcoming work will focus on a dynamic study of these hybrid cycles, to address the coupling between chemical reaction kinetics and expansion devices. To this end, promising solid reactants will be chosen based on this preliminary study and on additional considerations, such as cost, toxicity, corrosiveness and feasibility criteria. Moreover, an experimental setup is in progress to validate the theoretical predictions of the thermodynamic analysis (energy and exergy performances) and the upcoming dynamic study. A scroll expander is already available, operable with ammonia and under the predicted operating pressures and temperatures.

Appendix A. Computation of molar heat capacities of the reactants

The energy balance equations listed in Section 3.1 require knowledge of some molar heat capacities to account for sensible heat of reactive salts. In this section, further details are provided on the computation of these thermodynamic properties. We note that subscripts 'an', 'p' and 'r' refer to 'anhydrous' reactant, 'poor' reactant (reactive salt after decomposition reaction) and 'rich' reactant (reactive salt after synthesis reaction), respectively. Therefore, the chemical reaction between solid reactive salt and gaseous ammonia is:

$$Salt_p + \nu . NH_3 \rightleftharpoons Salt_r$$

, where $Salt_p \equiv Salt_{an}.n_0 NH_3$
and $Salt_r \equiv Salt_{an}.(n_0 + \nu)NH_3$.

Firstly, molar heat capacities of anhydrous reactants and ammonia (at constant pressure) are provided:

- $C_{salt,an} = 70\ J.mol^{-1}.K^{-1}$ (fair approximation of molar heat capacities for the whole set of reactants).
- $C_{NH3} = 40\ J.mol^{-1}.K^{-1}$.

Then, molar heat capacities of 'poor' and 'rich' reactive salts are deduced, using the following equations:

- $C_{salt,p} = C_{salt,an} + n_o.C_{NH3}$.
- $C_{salt,r} = C_{salt,an} + (n_o + \nu).C_{NH3}$.

Appendix B. Additional results

B.1. Comparison between 'real' and 'perfect' simulation cases

As stated in Section 3.1, a set of values considered as 'realistic' has been defined for the key simulation parameters: $\eta_{is} = 0.8$, $\Delta X = 0.8$, $\tau_{met} = 0.1$, $\Delta T_{HX1} = 5$ K, $\Delta T_{HX2} = 10$ K and $\Delta T_{eq} = 20$ K. The results presented in Sections 4 and 5 were obtained under this *'real'* set of parameters. However, since the existing literature on hybrid thermochemical cycles [10-24] usually relies on more optimistic assumptions (especially for temperature pinches), a fair comparison of the performances of the proposed cycle with other hybrid thermochemical cycles cannot be provided. Therefore, another set of parameter values (more optimistic) has been defined and simulations have been carried out under this *'perfect'* set of parameters: $\eta_{is} = 1$, $\Delta X = 1$, $\tau_{met} = 0$, $\Delta T_{HX1} = 0$ K, $\Delta T_{HX2} = 0$ K and $\Delta T_{eq} = 0$ K. In this section, the results obtained under the *'perfect'* set of parameters are reported and a comparison with the *'real'* case is provided.

Firstly, in addition to *Figs. 10* and *14*, both 'perfect' (white symbols) and 'real' (solid symbols) energy and exergy efficiencies are displayed in *Figs. B1* (discharge power generation mode) and *B2* (combined mode). These plots highlight the high potential for improvement in the thermodynamic quality of the cycles.

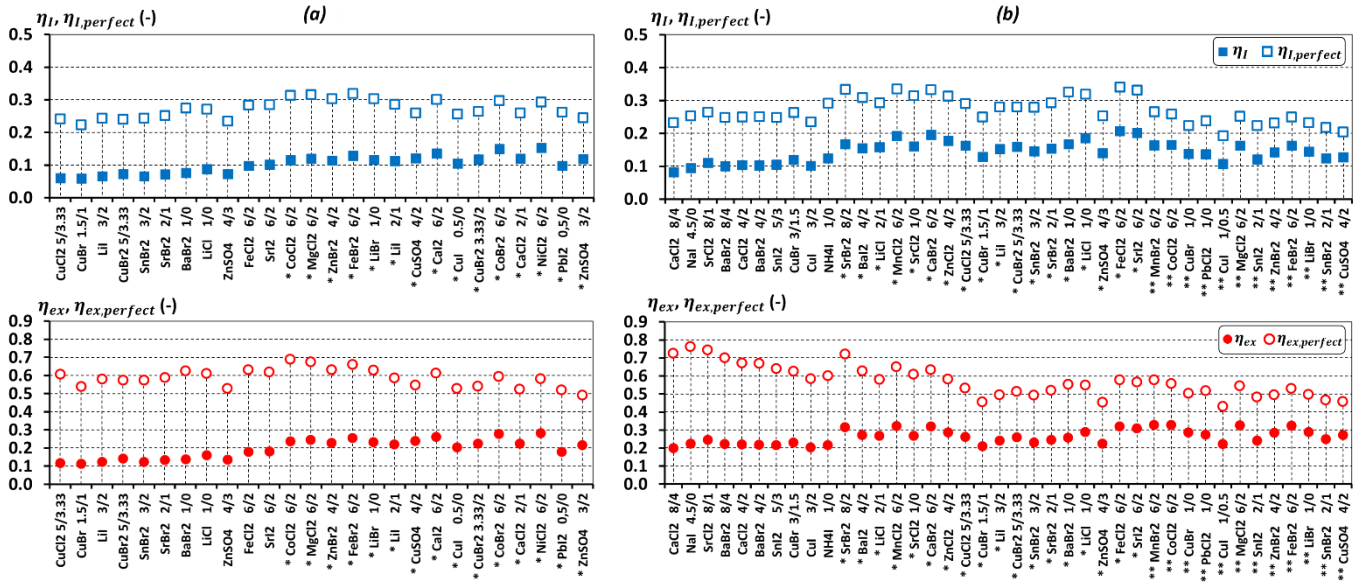

Fig. B1 – Discharge power generation mode: energy and exergy efficiencies of the cycle for selected salts (both 'perfect' and 'real' cases are plotted)

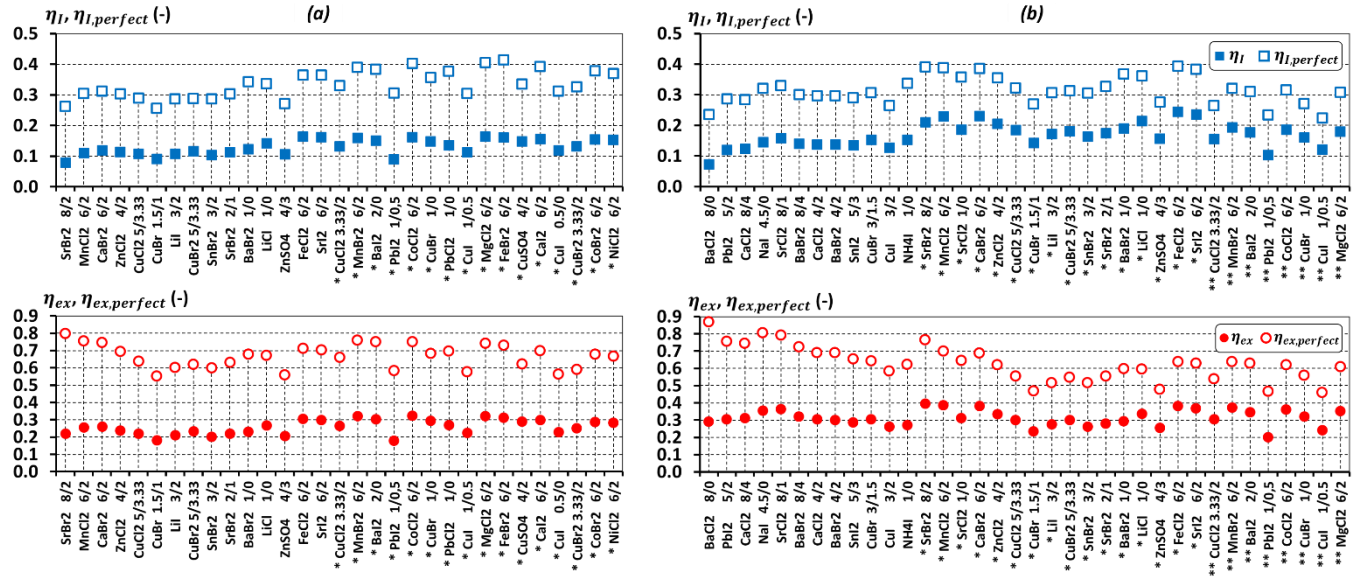

Fig. B2 – Combined power generation mode: energy and exergy efficiencies of the cycle for selected salts (both 'perfect' and 'real' cases are plotted)

The absolute deviations $\eta_I - \eta_{I,perfect}$ and $\eta_{ex} - \eta_{ex,perfect}$ and the relative deviations $(\eta_I - \eta_{I,perfect})/\eta_{I,perfect}$ and $(\eta_{ex} - \eta_{ex,perfect})/\eta_{ex,perfect}$ have been computed. The main results and observations are listed below:

- For the discharge power generation mode, relative deviations reach very high values for both energy and exergy efficiencies. The variation ranges are [−75.6; −34.9 %] for η_I, and [−80.7; −39.1 %] for η_{ex}. Absolute deviations are much higher for exergy efficiencies than for energy efficiencies: the respective variation ranges are [−0.54; −0.18] and [−0.20; −0.08]. This is because the variations of parameters ΔT_{HX1}, ΔT_{HX2} and ΔT_{eq} between 'perfect' and 'real' sets of assumptions strongly affect the heat source temperature T_{hot}, and so η_{ex} through the exergy input Ex_{in} (see Eqs. **(18)** and **(21)**).

- For the combined charge and discharge power generation mode, a high sensitivity to the set of assumptions is also observed: for relative deviations, the variation ranges are [−70.9; −37.9%] for η_I and [−72.6; −40.5%] for η_{ex}. We note that these relative deviations do not reach values as high as in discharge power generation mode, because the minimal values of η_I and η_{ex} in the 'real' case are higher.

The high values of relative deviations suggest that the performance may be greatly improved if parameter values are more favorable than in the 'real' case: in particular, the temperature pinches could be reduced to make an improvement. In conclusion, the discrepancies between 'real' and 'perfect' efficiencies indicate a high potential for improvement in the thermodynamic quality of these cycles. Further work is now needed: the distribution of irreversibilities among the components should be investigated in greater detail.

B.2. Operating conditions and performances plotted versus reactive HTSs

Operating conditions and performances of the cycles are summarized in *Figs. B3-B6* for all selected salts: heat source temperature T_{hot} and performance criteria η_I η_{ex} and $w+ex_{cold}$ are displayed. Instead of heat source temperature T_{hot}, the x-axis contains all selected salts for the two operating modes. We note that for each reactive salt, these variables were computed under the configuration using the least expansion stages.

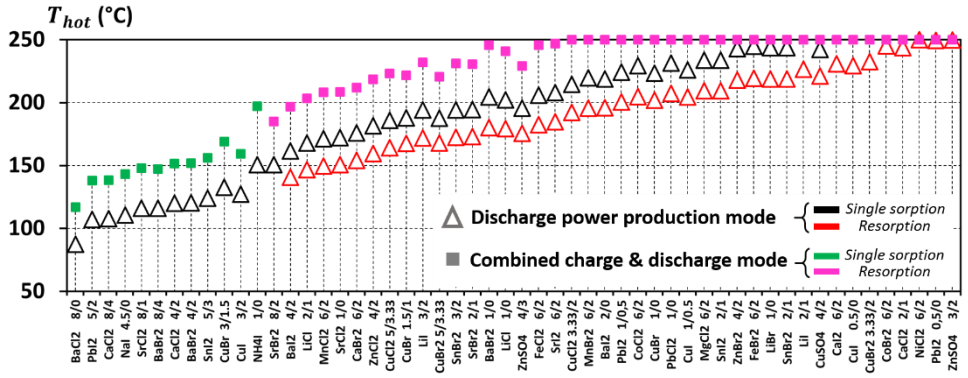

Fig. B3 – Heat source temperatures required for all selected salts in the 2 operating modes

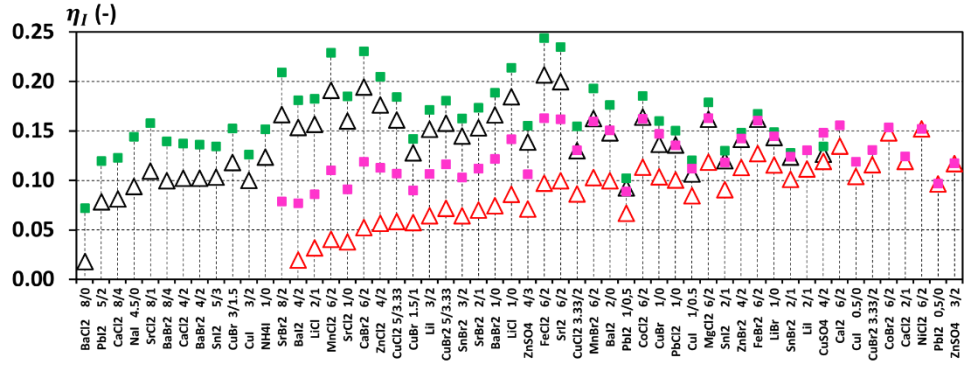

Fig. B4 – Energy efficiencies: summary of all selected salts in the 2 operating modes

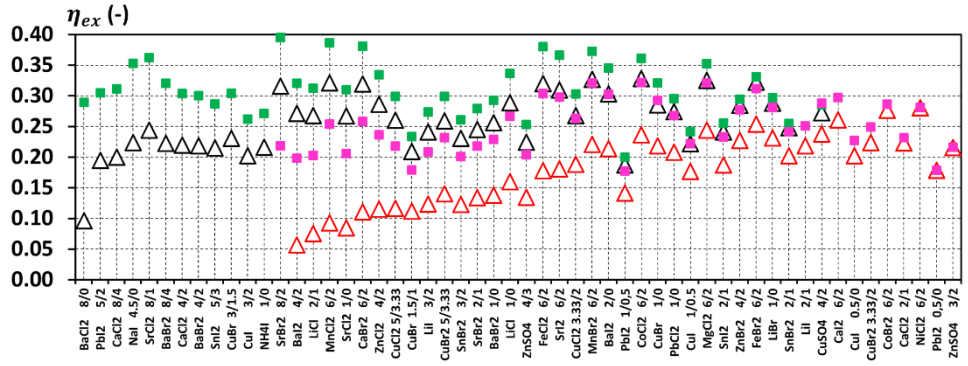

Fig. B5 – Exergy efficiencies: summary of all selected salts in the 2 operating modes

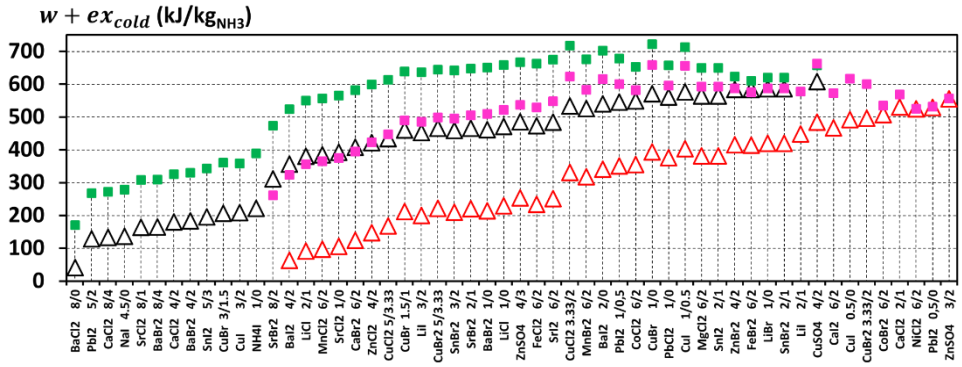

Fig. B6 – Specific exergy output: summary of all selected salts in the 2 operating modes

Acknowledgments

We warmly thank Pierre Neveu for his valuable help with thermodynamics. Alexis Godefroy is the recipient of a PhD grant from the French Ministry of National Education (doctoral contract No. 2017-09-ED.305).

References

[1] Ammar Y, Joyce S, Norman R, Wang Y, Roskilly AP. Low grade thermal energy sources and uses from the process industry in the UK. Applied Energy 2012;89:3-20.

[2] Roskilly AP, Yan J. Sustainable thermal energy management. Applied Energy 2017;186:249-50.

[3] Ling-Chin J, Bao H, Ma Z, Taylor W, Roskilly AP. (2019). State-of-the-Art Technologies on Low-Grade Heat Recovery and Utilization in Industry. In: Al-Bahadly IH, editor. Energy Conversion: Current Technologies and Future Trends; 2018, p. 55-73.

[4] Ziegler F, Jahnke A, Karow M. Re-evaluation of the Honigmann-process: thermo-chemical heat store for the supply of electricity and refrigeration. Vortrag und Proc. of the Heat Powered Cycles Conference, Berlin, 2009.

[5] Xu F, Goswami DY, Bhagwat S. A combined power/cooling cycle. Energy 2000;25:233-46.

[6] Tamm G, Goswami DY, Lu S, Hasan A. Theoretical and experimental investigation of an ammonia-water power and refrigeration thermodynamic cycle. Solar Energy 2004;76:217-28.

[7] Ayou DS, Bruno JC, Saravanan R, Coronas A. An overview of combined absorption power and cooling cycles. Renewable and Sustainable Energy Reviews 2013;21:728-48.

[8] Nadeem F, Hussain S, Tiwari P, Goswami AK, Ustun TS. Comparative Review of Energy Storage Systems, Their Roles and Impacts on Future Power Systems. IEEE Access 2019;7:4555-85.

[9] Aydin D, Casey SP, Riffat S. The latest advancements on thermochemical heat storage systems. Renewable and Sustainable Energy Reviews 2015;41:356-67.

[10] Wang L, Ziegler F, Roskilly AP, Wang R, Wang Y. A resorption cycle for the cogeneration of electricity and refrigeration. Applied Energy 2013;106:56-64

[11] Bao H, Wang Y, Charalambous C, Lu Z, Wang L, Wang R, Roskilly AP. Chemisorption cooling and electric power cogeneration system driven by low grade heat. Energy 2014;72:590-8

[12] Bao H, Wang Y, Roskilly AP. Modelling of a chemisorption refrigeration and power cogeneration system. Applied Energy 2014;119:351-62.

[13] Bao H, Ma Z, Roskilly AP. An optimised chemisorption cycle for power generation using low grade heat. Applied Energy 2017;186:251-61.

[14] Bao H, Ma Z, Roskilly AP. Integrated chemisorption cycles for ultra-low grade heat recovery and thermo-electric energy storage and exploitation. Applied Energy 2016;164:228-36.

[15] Bao H, Ma Z, Roskilly AP. Chemisorption power generation driven by low grade heat – Theoretical analysis and comparison with pumpless ORC. Applied Energy 2017;186:282-90.

[16] Bao H, Ma Z, Roskilly AP. A chemisorption power generation cycle with multi-stage expansion driven by low grade heat. Energy Conversion and Management 2017;150:956-65.

[17] Lu Y, Roskilly AP, Wang Y, Wang L. Study of a novel dual-source chemisorption power generation system using scroll expander. Energy Procedia 2017;105:921-26.

[18] Lu Y, Roskilly AP, Tang K, Wang Y, Jiang L, Yuan Y, et al. Investigation and performance study of a dual-source chemisorption power generation cycle using scroll expander. Applied Energy 2017;204:979-93.

[19] Lu Y, Bao H, Yuan Y, Wang Y, Wang L, Roskilly AP. Optimisation of a novel resorption cogeneration using mass and heat recovery. Energy Procedia 2014;61:1103-6.

[20] Lu Y, Wang Y, Bao H, Yuan Y, Wang L, Roskilly AP. Analysis of an optimal resorption cogeneration using mass and heat recovery processes. Applied Energy 2015;160:892-901.

[21] Lu Y, Wang Y, Wang L, Yuan Y, Liu Z, Roskilly AP. Experimental investigation of a scroll expander for power generation part of a resorption cogeneration. Energy Procedia 2015;75:1027-32.

[22] Jiang L, Wang LW, Liu CZ, Wang RZ. Experimental study on a resorption system for power and refrigeration cogeneration. Energy 2016;97:182-90.

[23] Jiang L, Lu YJ, Roskilly AP, Wang RZ, Wang LW, Tang K. Exploration of ammonia resorption cycle for power generation by using novel composite sorbent. Applied Energy 2018;215:457-67.

[24] Jiang L, Roskilly AP, Wang RZ, Wang LW. Analysis on innovative resorption cycle for power and refrigeration cogeneration. Applied Energy 2018;218:10-21.

[25] Godefroy A, Perier-Muzet M, Mazet N. Thermodynamic analyses on hybrid sorption cycles for low-grade heat storage and cogeneration of power and refrigeration. Applied Energy 2019;255.

[26] Neveu P, Domblides JP, Castaing-Lasvignottes J. Diagrammes thermodynamiques relatifs aux équilibres solide / gaz. Proceedings of the International Ab-sorption Heat Pump Conference, Montréal, 1996:237-44.

[27] Touzain P. Thermodynamic values of ammonia-salts reactions for chemical sorption heat pumps. Proceedings of the International Sorption Heat Pump Conference, Munich, 1999:225-38.

[28] F-Chart Software: Engineering Software EES: Engineering Equation Solver. http://www.fchart.com/ees

[29] Wentworth WE, Johnston DW. Chemical heat pumps using a dispersion of a metal salt ammoniate in an inert solvent. Solar Energy 1981;26:141-6.

[30] Böhringer JM. Sur la thermodynamique et la cinétique de l'absorption et la désorption d'ammoniac par le chlorure de strontium. TM-42-80-3, Würenlingen, Switzerland.